AGU PUBLICATIONS

JGR

Journal of Geophysical Research: Oceans

RESEARCH ARTICLE

10.1002/2014JC010473

The "winter predictability barrier" for IOD events and its error growth dynamics: Results from a fully coupled GCM

Rong Feng[1], Wansuo Duan[1], and Mu Mu[2]

[1]LASG, Institute of Atmospheric Physics, Chinese Academy of Sciences, Beijing, China, [2]Key Laboratory of Ocean Circulation and Wave, Institute of Oceanology, Chinese Academy of Sciences, Qingdao, China

Key Points:
- Demonstrating the existence of the WPB under the effects of initial errors
- Explaining the physical mechanism of the WPB from perspective of error growth

Correspondence to:
W. Duan,
duanws@lasg.iap.ac.cn

Citation:
Feng, R., W. Duan, and M. Mu (2014), The "winter predictability barrier" for IOD events and its error growth dynamics: Results from a fully coupled GCM, *J. Geophys. Res. Oceans*, *119*, doi:10.1002/2014JC010473.

Received 23 SEP 2014
Accepted 26 NOV 2014
Accepted article online 29 Nov 2014

Abstract Within the Geophysical Fluid Dynamics Laboratory Climate Model version 2p1 (GFDL CM2p1) coupled model, we find that the winter predictability barrier (WPB) exists in both the growing and decaying phases of positive Indian Ocean dipole (IOD) events, due to the effects of initial errors. The physical mechanism of the WPB, in which the initial errors show a significant seasonal-dependent evolution with the fastest error growth in winter, is explored from the dynamical and thermodynamical viewpoints. In terms of dynamics, in the growing phase of pure positive IOD events, the vertical temperature advection associated with the reference state IOD events plays a dominant role in advancing the fastest error growth in winter; in terms of thermodynamics, the latent heat flux error and the shortwave radiation error lead to the fastest error growth in winter and favor the occurrence of the WPB. In the decaying phase of pure positive IOD events, the occurrence of the WPB is mainly due to the latent heat flux error since the dynamics play an insignificant role in advancing the fast error growth in winter. For positive IOD events accompanied by El Niño-Southern Oscillation (ENSO), the physical mechanism of the WPB is similar to that for pure positive IOD events in both the growing and decaying phases, except that the shortwave radiation error has a different effect on the error growth in winter, which may be closely related to the perturbed atmospheric circulation in the tropical Indian Ocean associated with ENSO.

1. Introduction

The Indian Ocean dipole (IOD) is a prominent climate phenomenon in the tropical Indian Ocean [*Saji et al*., 1999; *Webster et al*., 1999; *Li et al*., 2003; *Saji and Yamagata*, 2003a; *Annamalai et al*., 2005]. Positive IOD events are characterized by positive sea surface temperature anomalies (SSTAs) in the western Indian Ocean and negative SSTAs in the southeastern Indian Ocean, with easterly winds at the equator [*Saji et al*., 1999; *Webster et al*., 1999; *Murtugudde et al*., 2000; *Li et al*., 2002, 2003]. Positive IOD events usually cause a large amount of rain in east Africa, and severe drought in Indonesia and Australia [*Birkett et al*., 1999; *Ansell et al*., 2000; *Ashok et al*., 2001; *Black et al*., 2003; *Clark et al*., 2003; *Lareef et al*., 2003; *Yamagata et al*., 2004; *Behera et al*., 2005]. These events also have close links with the monsoon and could affect global climate via Rossby wave activity [*Ansell et al*., 2000; *Black et al*., 2003; *Guan and Yamagata*, 2003; *Saji and Yamagata*, 2003b; *Annamalai and Murtugudde*, 2004; *Vecchi and Harrison*, 2004]. Negative IOD events are characterized by the opposite SSTA patterns and climate effects to positive IOD events. Whether or not the IOD is independent of El Niño-Southern Oscillation (ENSO) is the subject of much debate [*Saji et al*., 1999; *Webster et al*., 1999; *Li et al*., 2003; *Behera et al*., 2006]. The IOD index, which is the difference in SSTA between the western Indian Ocean (50°E–70°E, 10°S–10°N) and southeastern Indian Ocean (90°E–110°E, 10°S–Equator) [*Saji et al*., 1999], is usually used to measure the strength of IOD events. An IOD event is said to occur when the absolute value of the IOD index exceeds 0.5 standard deviations for three consecutive months [*Song et al*., 2007]. The occurrence, peak, and decay of IOD events are often phase-locked to the seasonal cycle, which is a very important characteristic of IOD events [*Saji et al*., 1999; *Webster et al*., 1999; *Li et al*., 2002, 2003; *Krishnamurthy and Kirtman*, 2003; *Saji and Yamagata*, 2003a; *Lau and Nath*, 2004; *Shinoda et al*., 2004; *Cai et al*., 2005; *Zhong et al*., 2005; *Behera et al*., 2006]. Previous studies have shown that IOD events often reverse the sign of the IOD index during the preceding winter, then peak in September or October in the IOD year, and at last reverse the sign again in the following winter; this occurs both in model output and in the NCEP/NCAR reanalysis data [*Wajsowicz*, 2004]. This indicates that the winter season, in which IOD events often appear and disappear, is an important period in the lifetime of IOD events.

As IOD events have significant effects on climate both locally and remotely, it is important to be able to predict IOD events in advance, especially their appearance and disappearance, which mostly occur in winter. *Wajsowicz* [2004, 2005, 2007] analyzed the predictability of SSTAs related to IOD events, and demonstrated the existence of the winter persistence barrier in IOD events, which indicates that the memory of the SSTA variation is weakest in winter and that the persistence forecast skill declines rapidly across winter. By analyzing the observation data and the Coupled Model Intercomparison Project Phase 5 (CMIP5) model output, *Feng et al*. [2014] found that the winter persistence barrier exists not only in the growing phase of IOD events but also in the decaying phase. They also showed that the strongest dynamical coupling instability in winter favors the fastest growth of IOD events, resulting in the winter persistence barrier. It should be noted that the strongest dynamical coupling instability may also favor the fastest growth of perturbations (i.e., prediction errors) in winter [*Webster*, 1995], resulting in the occurrence of the winter predictability barrier (WPB). *Luo et al*. [2007] computed the anomaly correlation coefficients (ACCs) between the IOD index of observations and that of the Scale Interaction Experiment-Frontier Research Center for Global Change (SINTEX-F) model predictions. They found that, regardless of the start month, the ACCs drop rapidly across the boreal winter, indicating the existence of the WPB. The existence of the WPB may greatly restrict the lead time for the skillful prediction of IOD events, which is only about 1–2 seasons [*Wajsowicz*, 2004, 2005; *Luo et al*., 2005, 2007; *Zhao and Hendon*, 2009; *Shi et al*., 2012]. In addition, since IOD events usually appear and disappear in winter, the rapid drop in forecast skill caused by the WPB may lead to failures in forecasting the appearance and disappearance of IOD events, leading in turn to large socioeconomic losses. As a result, it is important to study the physical mechanism of the WPB and to determine how and to what extent the WPB can be weakened. In this study, we mainly focus on the physical mechanism of the WPB; the remaining questions are discussed in future work.

The spring predictability barrier (SPB) is a well-known phenomenon of ENSO in the tropical Pacific Ocean. The physical mechanism of the SPB has been studied from several perspectives, such as the effect of the monsoon [*Webster and Yang*, 1992; *Lau and Yang*, 1996] and the signal-to-noise ratio [*Torrence and Webster*, 1998]. Recently, *Mu et al*. [2007] revealed the initial errors that cause a significant SPB for El Niño by using an approach of conditional nonlinear optimal perturbation [see *Mu et al*., 2003]. *Duan et al*. [2009] showed that the evolving mode of the initial errors that are most likely to cause the SPB for ENSO is similar to the evolving mode of ENSO, in which the Bjerknes positive feedback plays an important role [also see *Yu et al*., 2009]. In light of the similarities in coupling characteristics between IOD events and ENSO, such as the active forcing role of the tropical ocean on the atmosphere and the Bjerknes positive feedback during the growth of events [*Vinayachandran et al*., 2002; *Li et al*., 2003], we study the WPB of IOD events from the viewpoint of initial error growth.

To investigate the effect of initial errors on WPB-related prediction uncertainties for IOD events, we conduct perfect model predictability experiments, in which the prediction errors are caused only by initial errors. Under this assumption, two questions are required to answer:

1. Does the WPB for IOD events (in which the prediction errors show a strong seasonal-dependent development with the fastest error growth in winter) exist in the Geophysical Fluid Dynamics Laboratory Climate Model version 2p1 (GFDL CM2p1) coupled general circulation model (GCM) under the effect of initial errors?
2. What are the roles of the dynamics and thermodynamics in the seasonal-dependent error growth related to the WPB?

As positive IOD events have larger magnitude, greater impacts on climate, and more frequent occurrence under climate change than negative IOD events [*Ashok et al*., 2001, 2003; *Vinayachandran et al*., 2002; *Abram et al*., 2003; *Black et al*., 2003; *Annamalai and Murtugudde*, 2004; *Yamagata et al*., 2004; *Behera et al*., 2005; *Hong et al*., 2008; *Cai et al*., 2009; *Weller and Cai*, 2013], we only consider positive IOD events in this study (i.e., where the IOD index exceeds 0.5 standard deviations for three consecutive months); negative IOD events will be the subject of future work.

The remainder of this paper is organized as follows: the model is described in section 2, and section 3 presents the experimental strategy and demonstrates the existence of the WPB for positive IOD events in the GFDL CM2p1 coupled model under the effect of initial errors. In section 4, the physical mechanism of the WPB in different developmental phases of positive IOD events is explored from the viewpoints of dynamics and thermodynamics. Finally, a summary and discussion are presented in section 5.

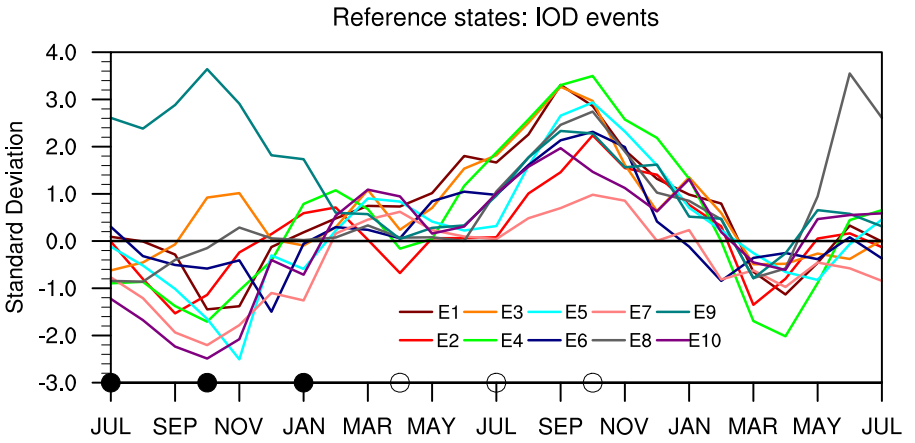

Figure 1. IOD indexes of 10 positive IOD events used in this study. E1–E10 denote the IOD events with the model year 1, 3, 11, 20, 59, 81, 88, 90, 92, 95, respectively. The filled circles signify the start months 7(−1), 10(−1), and 1(0) ("−1" signifies the year preceding the IOD year; "0" signifies the IOD year), and the integrations from these start months bestride the winter in the growing phase of positive IOD events; the hollow circles signify the start months 4(0), 7(0), and 10(0), and the predictions from these start months bestride the winter in the decaying phase of positive IOD events.

2. Model

In this study, the GFDL CM2p1 coupled model, which contains an ocean model, an atmosphere model, a land model, and a sea ice model, is used to explore the physical mechanism of the WPB for positive IOD events. The basic characteristics of the GFDL CM2p1 coupled model are introduced below; for more details, see *Griffies* [2009] or papers about the CM2.1 model (which has a comparable simulation skill to that of the CM2p1 model), such as *Gnanadesikan et al*. [2006], *Delworth et al*. [2006], *Wittenberg et al*. [2006], and *Stouffer et al*. [2006].

The ocean component of the GFDL CM2p1 coupled model is the Modular Ocean Model version 4 (MOM4p1) [*Griffies*, 2009], which was released in 2009 and is the main difference between the CM2p1 and CM2.1 versions of the model. MOM4p1 is a numerical representation of the ocean's hydrostatic primitive equations, with a horizontal resolution of $1^\circ \times 1^\circ$ in most regions and with the meridional resolution reducing to $1/3^\circ$ near the equator. There are 50 vertical levels in total with a 10 m resolution in the upper 225 m. The atmosphere component is the GFDL atmosphere model AM2p12b [*GFDL Global Atmospheric Model Development Team*, 2004], and it has a resolution of 2° latitude by 2.5° longitude with 24 vertical levels. The different components of the model are coupled using the GFDL's Flexible Modeling System (FMS, http://www.gfdl.noaa.gov/fms) and exchange fluxes every 2 h.

The GFDL CM2p1 coupled model is run for 150 years, forced by 1990 values of aerosols, land cover, tracer gases, and insolation. After a 50 year spin-up, the last 100 years are analyzed to eliminate the effect of initial adjustment processes. Figure 1 shows the IOD indexes of 10 positive IOD events randomly chosen from the 100 year integration in the GFDL CM2p1 coupled model. In most cases, the sign of the IOD index is reversed from negative to positive in the winter season (January (0) to March (0), where "0" indicates the IOD year), then peaks in September (0) or October (0), and finally its sign is reversed again in the following winter (January (1) to March (1), where "1" indicates the year following the IOD year). The phase-locking characteristic of the positive IOD events in the GFDL CM2p1 coupled model is consistent with that in observations [*Wajsowicz*, 2004]. Furthermore, *Feng et al*. [2014] assessed the simulation skill of the tropical Indian Ocean climatology in 14 CMIP5 models by comparing model results with observations, using four quantities: the variance of the IOD index, the climatological zonal sea surface temperature (SST) gradient, climatological annual zonal winds at 10 m at the equator, and the climatological annual thermocline depth in the tropical Indian Ocean. Among the 14 coupled models, the GFDL CM2p1 coupled model was found to simulate the seasonal cycle well, which indicates that the model has a high simulation capability for the climatology in the tropical Indian Ocean. They also showed that the winter persistence barrier exists in the GFDL CM2p1 coupled model in both the growing and decaying phases of positive IOD events, in accordance with observations. The high simulation skill of the GFDL CM2p1 coupled model on the climatology and interannual

variability of the tropical Indian Ocean motivates the further study of IOD events with the GFDL CM2p1 model, as presented in the following sections.

3. Existence of the WPB in the GFDL CM2p1 Coupled Model and Its Related Initial Errors

3.1. Experimental Strategy

In the perfect model predictability experiments, the GFDL CM2p1 coupled model is assumed to be perfect and the prediction errors are caused only by initial errors. The 10 positive IOD events randomly chosen from the 100 year integration (Figure 1) are regarded as the "true states" (i.e., reference states) to be predicted, and their predictions are obtained by integrating the model with perturbed initial fields. As the ocean actively forces the atmosphere in the tropical Indian Ocean, the initial uncertainty is only superimposed on the sea temperature. However, initial errors are not added to all levels of sea temperature in the GFDL CM2p1 coupled model because such initial perturbations will probably result in the incompatibility between the initial fields and the model. This incompatibility may cause robust initial shock, and in turn conceal the effect of initial errors on the prediction uncertainties of IOD events, especially in the first few months. Considering the fact that the mean thermocline depth is about 110–130 m in the tropical Indian Ocean [*Song et al*., 2007], the sea temperature anomalies at the sea surface and 95 m depth can reflect the variation of the SST and thermocline depth to some extent, which are closely related to the evolution of IOD events [*Rao et al*., 2002; *Vinayachandran et al*., 2002]. Then initial perturbations on these two levels could probably reflect the effect of sea temperature perturbations on the prediction uncertainties of positive IOD events. Based on the above discussions, initial errors are therefore only superimposed on sea temperatures at the sea surface and at 95 m depth in the reference state IOD events in our study.

Previous studies have demonstrated that the initial errors causing significant prediction uncertainties for coupled ocean-atmospheric modes (e.g., ENSO events, Kuroshio Large Meander, Atlantic and Pacific blockings, etc.) may have dynamical growth behavior similar to the events themselves [*Yu et al*., 2009; *Jiang and Wang*, 2010; *Duan et al*., 2012; *Wang et al*., 2012]. Besides, *Duan et al*. [2009] demonstrated that such kinds of initial errors for ENSO events would be most likely to cause a significant "spring predictability barrier." These results encourage us to investigate the WPB of IOD events by superimposing initial errors derived from IOD-related sea temperature anomalies. Moreover, the 4 years dominant period of IOD events in the GFDL CM2p1 coupled model [*Feng and Duan*, 2014] means that there are usually a positive IOD event and a negative IOD event within 4 years; therefore, the patterns of sea temperature anomalies within 4 years are plentiful. So we sample the SSTAs and temperature anomalies at 95 m depth in the tropical Indian Ocean every other month from the 4 years preceding each reference state IOD event to make initial sea temperature errors as many as possible; that is, there are 24 pairs of initial errors altogether for each positive IOD event. After adjusting these initial errors to the same magnitude, we superimpose them onto the initial fields of the reference state IOD events and integrate them from six start months for 12 months. That is to say, for each start month, we totally conduct 240 predictions (10 IOD events multiplied by 24 initial errors). The integrations with start months 7 (−1) ("−1" signifies the year preceding the IOD year), 10 (−1), and 1 (0) ("0" signifies the IOD year) bestride the winter in the growing phase of positive IOD events, and integrations with start months 4 (0), 7 (0), and 10 (0) bestride the winter in the decaying phase of positive IOD events (Figure 1). The definitions of the growing and decaying phases of positive IOD events are given by *Feng et al*. [2014].

Specific steps are as follows. The original SSTAs and temperature anomalies at 95 m depth are labeled as T_1 and T_2, with T_{1ij} and T_{2ij} indicating values of T_1 and T_2 at grid point (i, j) in the region with longitude ranging from 45°E to 115°E and latitude from 10°S to 10°N. To impartially compare the relative importance of different initial errors on the predictability of positive IOD events, T_1 and T_2 are scaled by $T_{10} = T_1/\delta_1$ and $T_{20} = T_2/\delta_2$ (where δ_1 and δ_2 represent positive values) to obtain the same magnitude, respectively. T_{10} and T_{20} are the initial errors superimposed on the "true states" of the positive IOD events. The magnitudes of these initial errors are constrained by the norms $\|T_{10}\| = \sqrt{\sum_{i,j}(T_{10ij})^2}$ and $\|T_{20}\| = \sqrt{\sum_{i,j}(T_{20ij})^2}$, which are set as 2.4°C in our study. *Kaplan et al*. [1998] showed that the standard deviation of analysis errors (i.e., the difference between the initial analysis fields and the observations) of SSTAs along the equator is 0.2°C, which is larger than the initial error at any grid point (i, j) in the tropical Indian Ocean. This finding indicates

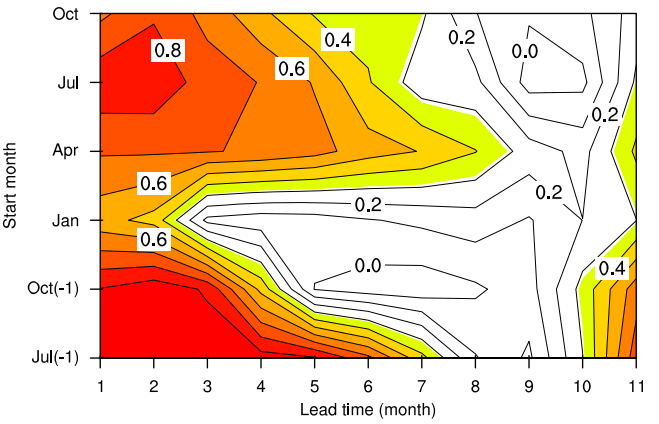

Figure 2. Anomaly correlation coefficients (ACCs) between the IOD indexes of 10 reference state positive IOD events and those of the predicted IOD events with different initial errors as a function of the start months and lead times. The contour interval is 0.1. ACCs significant at the 0.05 level are colored. A 5 month running mean is applied to remove the effect of intraseasonal time scales.

that the initial errors analyzed in our study may exist in the analysis errors and that the magnitude of our initial errors is reasonable.

3.2. Existence of the WPB in the GFDL CM2p1 Coupled Model

Luo et al. [2007] conducted an ACC analysis of the IOD index between SINTEX-F model output and observations. They found that regardless of the start month, the ACC declines rapidly across the winter season, indicating the existence of the WPB for IOD events in the SINTEX-F coupled model under the combined effects of model errors and initial errors. As the perfect model predictability experiments conducted in our study only consider initial errors, it is of great interest to determine whether the WPB of IOD events exists in the GFDL CM2p1 coupled model under the effect of initial errors alone.

An ACC analysis similar to that of *Luo et al.* [2007] is applied between the "observations" and "predictions" in our study. The IOD indexes of the 10 original positive IOD events are calculated as "observations"; the IOD indexes predicted after randomly superimposing four pairs of initial errors out of the 24 pairs (described in section 3.1) onto each positive IOD event and integrating from six different start months are considered to be the corresponding "predictions." That is to say, we conduct four predictions for each initial condition and there are totally 40 predictions for each start month. The ACCs between the 40 "predictions" and the corresponding 40 "observations" (only 10 nonduplicated observations) are then calculated for each start month after obtaining a 5 month running mean, which removes the effect of the intraseasonal signals (Figure 2). Regardless of the start month, the correlation coefficients decline quickly across the boreal winter in the growing phase of positive IOD events, indicating a rapid drop in the forecast skill in winter and the occurrence of the WPB in the growing phase of positive IOD events; similarly, the WPB exists in the decaying phase, but it is weaker than that in the growing phase. The results indicate that the predictability is lower in the winter of the growing phase than in the decaying phase and that the occurrence of the positive IOD events may be more difficult to forecast than their decay. These results suggest that initial errors that are superimposed only on the sea temperatures at the sea surface and at 95 m depth can cause the WPB of positive IOD events in the GFDL CM2p1 coupled model. This also indicates that the initial errors in the sea temperature strongly influence the predictability of positive IOD events, which motivates us to explore the sensitive areas of positive IOD predictions from the sea temperature of the sea surface and at 95 m depth in a future study.

3.3. Initial Errors That are Most Likely to Cause the WPB of Positive IOD Events

The above analysis shows that the WPB exists in the GFDL CM2p1 coupled model not only in the growing phase of positive IOD events but also in the decaying phase. The initial errors that are most likely to cause the occurrence of the WPB in the coupled model, and that show a strong seasonal-dependent growth with its fastest growth in winter, will be chosen according to the following description.

For each start month, 24 pairs of initial errors are superimposed on the "true state" of every positive IOD event; i.e., 24 predictions are obtained for each positive IOD event after a 12 month integration. The absolute value of the difference in IOD index between the prediction and the corresponding "true state" of the positive IOD event is seen as a prediction error, which is written as $\gamma=|TT'|$, where TT' is the difference in IOD index between the prediction and the "true state" of the positive IOD event. Each calendar year is divided into four "seasons," with January–March as the boreal winter, April–June as the boreal spring, and so on. The slope κ_n of γ in the nth month is roughly estimated by $\kappa_n=(\gamma_{n+1}-\gamma_{n-1})/(t_{n+1}-t_{n-1})$, where $\gamma(t_{n-1})$ is the prediction error in the preceding month t_{n-1} and $\gamma(t_{n+1})$ is the prediction error in the

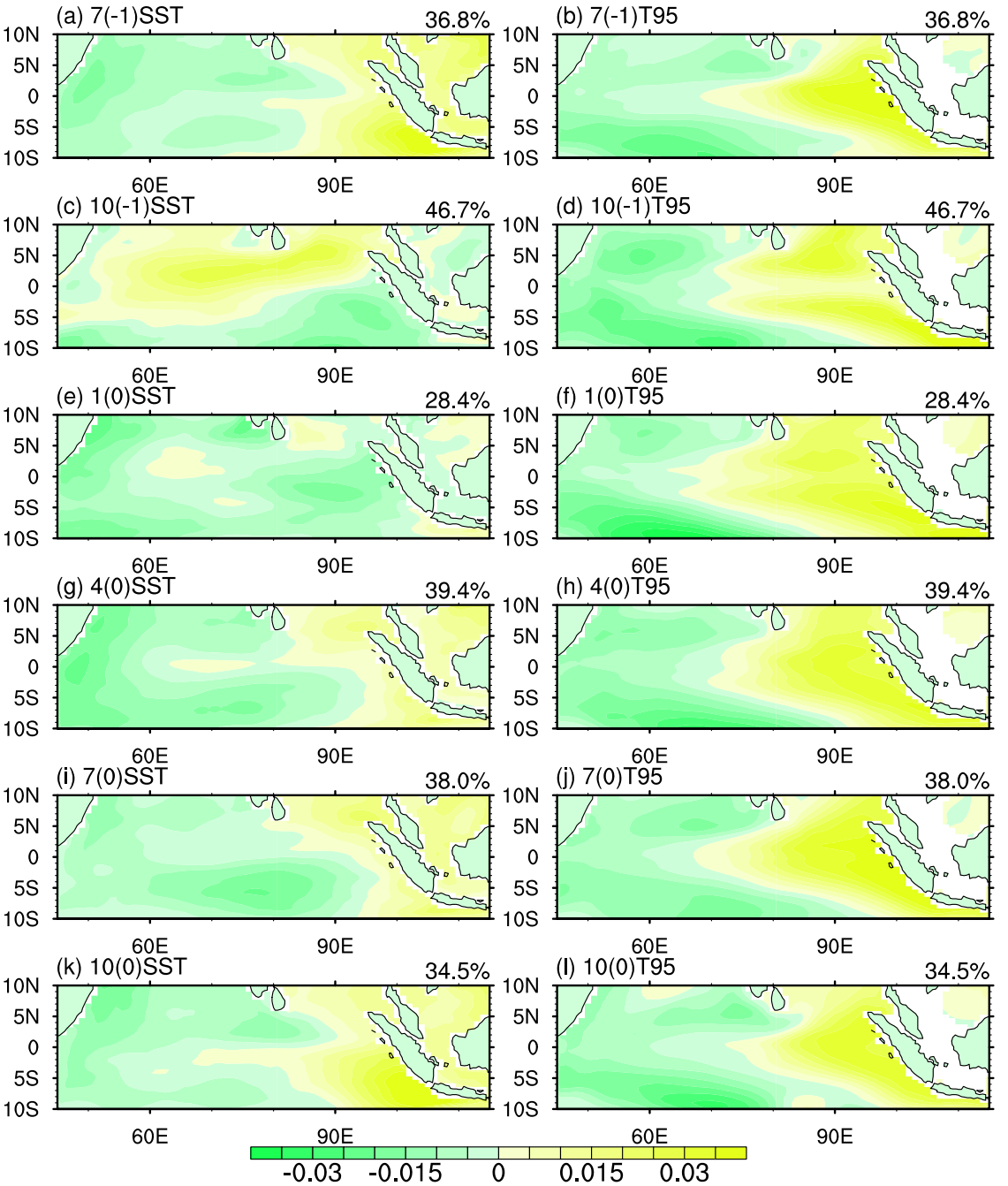

Figure 3. (left) The sea surface temperature errors of CEOF1 for initial errors that are most likely to cause the occurrence of the WPB with start months of (a) 7(−1), (c) 10(−1), (e) 1(0), (g) 4(0), (i) 7(0), and (k) 10(0). (right) The sea temperature errors at the 95 m depth of the CEOF1 for the corresponding start month (units: °C).

following month t_{n+1}; the mean value of κ for each season represents the growth rate of the prediction error for the season. A positive value of κ indicates an increase in the prediction errors for a given season, and a negative value of κ indicates a decrease; the larger the positive value of κ, the faster the prediction error grows in that season. For each initial error superimposed on the "true state" of a positive IOD event, four values of κ are obtained (one for each season), of which the largest positive value of κ is labeled as κ_{max} and the second largest as $\kappa_{s\text{-}max}$. If $\kappa_{max} > 0.375$ (the largest 10%) and κ_{max}-$\kappa_{s\text{-}max} > 0.06$, the error growth at the season corresponding to κ_{max} is considerably larger than that at other seasons. As the initial

errors closely related to the WPB show a strong seasonal-dependent growth with the fastest growth in winter, initial errors that cause κ_{max} in winter are selected as those that are most likely to cause the WPB of positive IOD events in the GFDL CM2p1 coupled model. We analyze the dominant pattern of the selected initial errors with Combined Empirical Orthogonal Functions (CEOF) analysis (Figure 3) [also see *Feng and Duan*, 2014]. The results show that, for most start months, the dominant pattern presents an eastern-western dipole both at the surface and at 95 m depth, and its large values concentrate within a few areas. Furthermore, we also analyze the growth of these initial errors (i.e., TT'; Figure 4). Apparently, the absolute values of TT' increase rapidly in winter, which indicates the fastest growth of the prediction errors γ in winter and the occurrence of the significant WPB. In the next section, the physical mechanism of the WPB will be examined based on these selected initial errors.

4. Physical Mechanism of the WPB in the GFDL CM2p1 Coupled Model

In the previous section, initial errors that are most likely to cause the occurrence of the WPB were selected and were found to show a seasonal-dependent evolution, with the fastest growth in winter in both the growing and the decaying phases of positive IOD events. In this section, the physical mechanisms that favor the fastest error growth in winter are discussed by analyzing the sea temperature tendency equation from the dynamical and thermodynamical viewpoints. For convenience, only the integrations with start months of 7 (−1) and 7 (0) are considered; these represent the integration cases bestriding the winter season in the growing and decaying phases of positive IOD events, respectively.

The following equations, which are used to explain the reasons for the fastest error growth in winter, are detailed below:

$$\frac{\partial T}{\partial t}=-u\frac{\partial T}{\partial x}-v\frac{\partial T}{\partial y}-w\frac{\partial T}{\partial z}+\frac{1}{\rho C_P}\frac{\partial Q}{\partial z}+\kappa\nabla^2 T \tag{1}$$

$$\begin{aligned}\frac{\partial(\overline{T}+T^*+T')}{\partial t}=&-(\overline{u}+u^*+u')\frac{\partial(\overline{T}+T^*+T')}{\partial x}-(\overline{v}+v^*+v')\frac{\partial(\overline{T}+T^*+T')}{\partial y}\\&-(\overline{w}+w^*+w')\frac{\partial(\overline{T}+T^*+T')}{\partial z}+\frac{1}{\rho C_P}\frac{\partial(\overline{Q}+Q^*+Q')}{\partial z}+\kappa\nabla^2(\overline{T}+T^*+T')\end{aligned} \tag{2}$$

$$\begin{aligned}\frac{\partial(\overline{T}+T^*)}{\partial t}=&-(\overline{u}+u^*)\frac{\partial(\overline{T}+T^*)}{\partial x}-(\overline{v}+v^*)\frac{\partial(\overline{T}+T^*)}{\partial y}-(\overline{w}+w^*)\frac{\partial(\overline{T}+T^*)}{\partial z}\\&+\frac{1}{\rho C_P}\frac{\partial(\overline{Q}+Q^*)}{\partial z}+\kappa\nabla^2(\overline{T}+T^*)\end{aligned} \tag{3}$$

$$\frac{\partial T'}{\partial t}=D+H+R \tag{4}$$

in which

$$D=(\overline{U}+\overline{V}+\overline{W})+(U^*+V^*+W^*)+(U'+V'+W') \tag{5}$$

$$\begin{aligned}&\bar{U}=-\bar{u}\frac{\partial T'}{\partial x}-u'\frac{\partial\bar{T}}{\partial x} \quad \bar{V}=-\bar{v}\frac{\partial T'}{\partial y}-v'\frac{\partial\bar{T}}{\partial y} \quad \bar{W}=-\bar{w}\frac{\partial T'}{\partial z}-w'\frac{\partial\bar{T}}{\partial z}\\&U^*=-u^*\frac{\partial T'}{\partial x}-u'\frac{\partial T^*}{\partial x} \quad V^*=-v^*\frac{\partial T'}{\partial y}-v'\frac{\partial T^*}{\partial y} \quad W^*=-w^*\frac{\partial T'}{\partial z}-w'\frac{\partial T^*}{\partial z}\\&U'=-u'\frac{\partial T'}{\partial x} \quad V'=-v'\frac{\partial T'}{\partial y} \quad W'=-w'\frac{\partial T'}{\partial z}\\&H=\frac{1}{\rho C_P}\frac{\partial Q'}{\partial z}\end{aligned} \tag{6}$$

$$\frac{\partial(\langle T'\rangle_{west}-\langle T'\rangle_{east})}{\partial t}=(\langle D\rangle_{west}-\langle D\rangle_{east})+(\langle H\rangle_{west}-\langle H\rangle_{east})+(\langle R\rangle_{west}-\langle R\rangle_{east}) \tag{7}$$

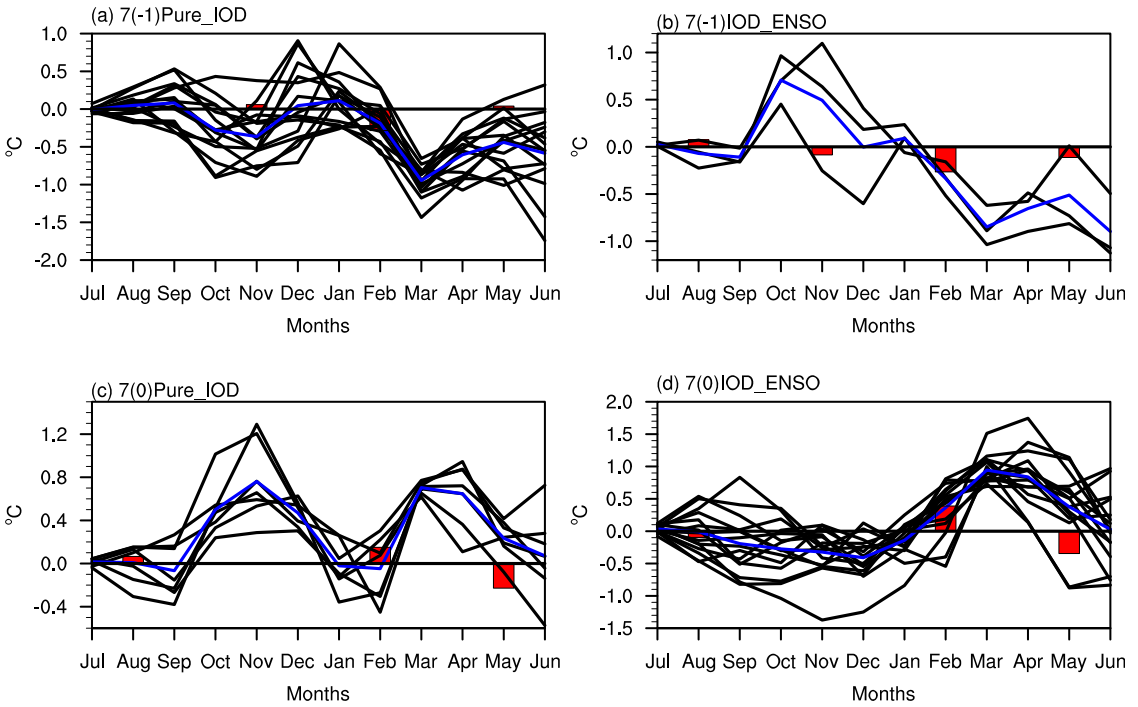

Figure 4. (a) Time-dependent evolutions of the difference in IOD index between the prediction and the "true state" of the positive IOD event (i.e., TT') for different initial errors that cause the occurrence of the WPB in the growing phase of pure positive IOD events, (b) in the growing phase of IOD events accompanied by ENSO, (c) in the decaying phase of pure positive IOD events, and (d) in the decaying phase of IOD events accompanied by ENSO (units: °C). Each black line denotes an individual prediction; the blue line indicates their composition. The total growth of prediction errors in different seasons are denoted by the red bars corresponding to August, November, February, and May in the horizontal axis, which are obtained by taking the ensemble mean of the average of the error growth tendencies in the corresponding seasons for the 15 predictions (units: °C/month).

Equation (1) is the sea temperature tendency equation at a given point, where T is the sea water temperature; u, v, and w are the zonal, meridional, and vertical current velocities, respectively; ρ is the sea water density, which is set to 1038 kg/m^3; C_P is the specific heat of sea water, which is set to 4000 J/(kg°C); and κ is the mixing coefficient. $Q=Q_{SW}+Q_{LW}+Q_{SH}+Q_{LH}$ is the net heat flux, which includes net shortwave radiation (Q_{SW}), net long wave radiation (Q_{LW}), sensible and latent heat fluxes (Q_{SH} and Q_{LH}); the shortwave radiation penetrating below the mixed layer is estimated using the equation for moderately clear water proposed by *Paulson and Simpson* [1977]. Each variable in equation (1) is divided into three terms in the form $X=\overline{X}+X^*+X'$, where $\overline{X}$ is the climatological mean of X, X^* denotes the anomaly of X in the reference state positive IOD events, and X' is the perturbation of X with the effects of superimposed initial errors. Inserting each expanded variable into equation (1) gives equation (2). Similarly, expanding each variable in equation (1) into two terms in the form $X=\overline{X}+X^*$ gives equation (3). Equation (4) is obtained by subtracting equation (3) from equation (2), where D, H, and R represent dynamical processes, thermodynamical processes, and the residual term, respectively. The dynamical processes term D in equation (5) represents the effect of temperature advection on the error growth, where $\overline{U}$, $\overline{V}$, and $\overline{W}$ represent the effect of zonal, meridional, and vertical temperature advection, respectively, associated with the climatology on the error growth; U^*, V^*, and W^* denote the effect of the temperature advection associated with the reference state IOD events on the error growth; and U', V', and W' represent the effect of the nonlinear interactions of temperature advection errors on the error growth. The thermodynamical processes term H in equation (6) represents the combined effect of the shortwave radiation error, the long wave radiation error, the sensible heat flux error, and the latent heat flux error on the error growth. The residual term R consists of mixing terms and truncation errors. We take the average of the terms in equation (4) within the mixed layer depth of the reference state IOD events, and denote these with "$\langle\rangle$" Equation (4) is then averaged over the western Indian Ocean (50°E–70°E, 10°S–10°N) and the eastern Indian Ocean (90°E–110°E, 10°S–Equator), and their difference is given by equation (7). The subscripts "west" and "east" signify the areal average of the terms over the western and eastern Indian Ocean, respectively. As the sign of TT' (i.e., the difference in IOD index between the prediction and the corresponding "true state") in each month during a season is almost the same for most

Table 1. Existence of ENSO (El Niño/La Niña) in the Winters of the Growing and Decaying Phases of 10 Positive IOD Events[a]

Reference IOD events	Growing Phase (January–March)	Decaying Phase (January–March)
1	La Nina	—
3	El Nino	El Nino
11	—	—
20	—	El Nino
59	La Nina	La Nina
81	—	El Nino
88	La Nina	El Nino
90	—	—
92	—	El Nino
95	La Nina	El Nino

[a]The first column denotes the 10 IOD years in the model. The words "El Niño" and "La Niña" indicate that the IOD events is accompanied by El Niño or La Niña in winter, respectively; the symbol "—" signifies that there is only IOD events in winter.

integrations (Figure 4), the seasonal growth rate of a prediction error $|TT'|$ can be roughly analyzed by calculating the seasonal growth rate of TT' (i.e., $\partial(\langle T'\rangle_{west}-\langle T'\rangle_{east})/\partial t$), which can be estimated approximately using equation (7). It is an approximation here because the SST is replaced with the mixed layer temperature. If the sign of TT' is the same as that of its growth rate ($\partial TT'/\partial t$, i.e., $\partial(\langle T'\rangle_{west}-\langle T'\rangle_{east})/\partial t$) in a season, the prediction error $|TT'|$ will increase in that season; otherwise, the prediction error $|TT'|$ will decrease. For simplicity, TT' is called the "prediction error" in the following discussion. Equation (7) therefore provides a measure of the processes governing the error growth rate from the following aspects: the effect of dynamics in the form of temperature advection, the effect of thermodynamics in the form of heat flux, and the effect of the residual term R.

Statistical analysis shows that positive IOD events are sometimes accompanied by La Niña in the winter of the growing phase, or accompanied by El Niño in the winter of the decaying phase (Table 1). It is natural to suppose that the physical mechanism of the WPB may be different for positive IOD events accompanied by ENSO in winter from those not accompanied by ENSO. Therefore, the physical mechanism of the WPB for positive IOD events only (called "pure IOD" in the later discussions) will be first discussed, and that for positive IOD events accompanied by ENSO in winter will be subsequently discussed in both sections 4.1 and 4.2 for different developmental phases.

4.1. Prediction Bestriding the Winter in the Growing Phase of Positive IOD Events

The integrations with start month 7 (−1) are analyzed to understand the physical mechanism of the WPB in the growing phase of positive IOD events. The discussion first considers pure positive IOD events, and subsequently positive IOD events accompanied by ENSO.

The prediction errors for pure positive IOD events are negative in most of the 12 months for most individual predictions, especially in their composition (Figure 4a), which may delay the occurrence of the predicted positive IOD events in winter. The fact that the error growth is fastest in winter indicates the occurrence of the WPB. The physical processes in equation (7) that cause the occurrence of the WPB are chosen and analyzed according to the following criteria: first, the physical processes term should be negative in winter, which is the same sign as for the prediction errors, i.e., the physical process promotes the error growth in winter; second, this promotion effect should be larger in winter than in other seasons; furthermore, based on the above criteria, only those physical processes whose magnitudes are larger than half of the error growth tendency are seen as significant and analyzed in this study. As the residual term R does not meet the second criterion (Figures 5a and 5b), we will explore the physical processes that favor the occurrence of the WPB from the viewpoints of dynamics and thermodynamics, respectively. Besides, in consideration of the consistency of the results for most individual predictions, the composite results are only shown in the following discussions.

4.1.1. Dynamics

Figure 6 shows the dynamical processes in different seasons for the mean of the 15 individual predictions superimposed with initial errors that are most likely to cause the occurrence of a significant WPB. It is apparent that the contribution of $\langle W^*\rangle$ to the error growth in winter is significantly larger than that of other oceanic dynamical processes, and favors the fastest error growth in winter. The vertical temperature advection associated with the reference state IOD events, denoted as $\langle W^*\rangle=-\langle w^*(\partial T'/\partial z)\rangle-\langle w'(\partial T^*/\partial z)\rangle$, can be written as $\langle W^*\rangle=W_1+W_2$, where $W_1=-\langle w^*(\partial T'/\partial z)\rangle$, $W_2=-\langle w'(\partial T^*/\partial z)\rangle$. W_1 and W_2 describe the vertical advection effect of the vertical velocity anomaly on the perturbed sea water temperature, and the vertical advection effect of the perturbed vertical velocity on the sea water temperature anomaly, respectively. The

contributions of W_1 and W_2 to the fast error growth in winter are similar to that of $\langle W^* \rangle$, indicating that both W_1 and W_2 advance the fastest error growth in winter and favor the occurrence of the WPB (Figure 7). Furthermore, W_1 (W_2) in the eastern Indian Ocean shows a strong seasonal-dependent distribution with the largest values located off the coast of Sumatra and Java in winter; in contrast, W_1 (W_2) in the western Indian Ocean is close to zero in every season (Figure 8). As the contribution of W_1 (W_2) to the growth rate of prediction errors depends on the difference in W_1 (W_2) between the western and eastern Indian Ocean (see equation (7)), W_1 (W_2) in the eastern Indian Ocean makes a large contribution to the fastest error growth in winter (which is also seen in Figure 9); in other words, W_1 and W_2 in the eastern Indian Ocean dominate the effect of $\langle W^* \rangle$ on the error growth and favor the occurrence of the WPB.

W_1 in the eastern Indian Ocean is determined by the vertical gradient of the perturbed sea water temperature $\langle \partial T'/\partial z \rangle$ and the anomalous vertical velocity $\langle w^* \rangle$. The vertical gradient of the perturbed sea water temperature in the eastern Indian Ocean is positive in winter, when its absolute value is significantly larger than in other seasons (Figure 10a). Accordingly, the anomalous vertical velocity is negative (i.e., downwelling) in winter, and in this season has the largest absolute value for most individual predictions (Figure 10c). The anomalous vertical movement of the sea water is closely related to the wind anomaly: the strong northwest wind anomaly in the eastern Indian Ocean in winter causes the accumulation of sea water close to the shore due to the Ekman effect, ultimately resulting in anomalous downwelling of the sea water (Figure 10e). The effect of the anomalous downwelling on the perturbed sea water with a positive vertical temperature gradient is favorable for warming the sea water in the eastern Indian Ocean, which in turn favors the fast growth of negative prediction errors in winter. As a result, the combination of the vertical gradient of the perturbed sea water temperature and the anomalous vertical velocity in the eastern Indian Ocean, which results in a seasonal-dependent distribution of W_1 with the largest value in winter, is favorable for the fastest error growth in winter.

Similarly, W_2 in the eastern Indian Ocean is also explored. W_2 is determined by the vertical gradient of the anomalous sea water temperature $\langle \partial T^*/\partial z \rangle$ and the perturbed vertical velocity $\langle w' \rangle$. Figure 10b shows that the vertical gradient of the anomalous sea water temperature in the eastern Indian Ocean is negative all year round, with the largest absolute value in winter. The perturbed vertical velocity in the eastern Indian Ocean is positive (i.e., upwelling) in winter with a larger absolute value than in other seasons (Figure 10d). As there is a close relationship between the perturbed wind under the effect of the superimposed initial errors and the perturbed vertical movement of the sea water, the perturbed wind is further analyzed. The perturbed southeast wind in the eastern Indian Ocean in winter results in offshore currents due to the Ekman effect, finally leading to a supplementary upwelling along the coast of Sumatra and Java in winter (Figure 10f). The effect of the perturbed upwelling on the anomalous sea water with a negative vertical temperature gradient results in the warming of sea water in the eastern Indian Ocean, and in turn induces the fastest growth of negative prediction errors in winter. The above discussions indicate that the combined effect of the vertical gradient of anomalous sea temperature and the perturbed vertical velocity in the eastern Indian Ocean, which results in a seasonal-dependent distribution of W_2 with its largest value in winter, contributes greatly to the dominant dynamical contribution of $\langle W^* \rangle$ to the seasonal-dependent development of prediction errors, with the fastest error growth in winter.

4.1.2. Thermodynamics

The previous section explored the physical mechanism of the WPB from the viewpoint of dynamics, and showed that the vertical temperature advection associated with the reference state positive IOD events plays a major role in advancing the fastest error growth in winter, resulting in the occurrence of the WPB. In this section, we continue these discussions from the viewpoint of thermodynamics.

Figure 11 shows the contributions of thermodynamical processes to the error growth from four aspects: the longwave radiation error, the shortwave radiation error, the latent heat flux error, and the sensible heat flux error; the quantities shown are the mean of the 15 individual predictions. It is apparent that the latent heat flux error and the shortwave radiation error are significantly larger than other thermodynamical processes in winter, and advance the fastest error growth during this season. Although the absolute value of the latent heat flux error in autumn is also large, it inhibits the error growth because of the opposite signs of the latent heat flux error and prediction errors; this is also the case for the shortwave radiation error in spring. As a result, the major thermodynamical processes that contribute to the occurrence of the WPB will be explored from the aspects of the latent heat flux error and the shortwave radiation error.

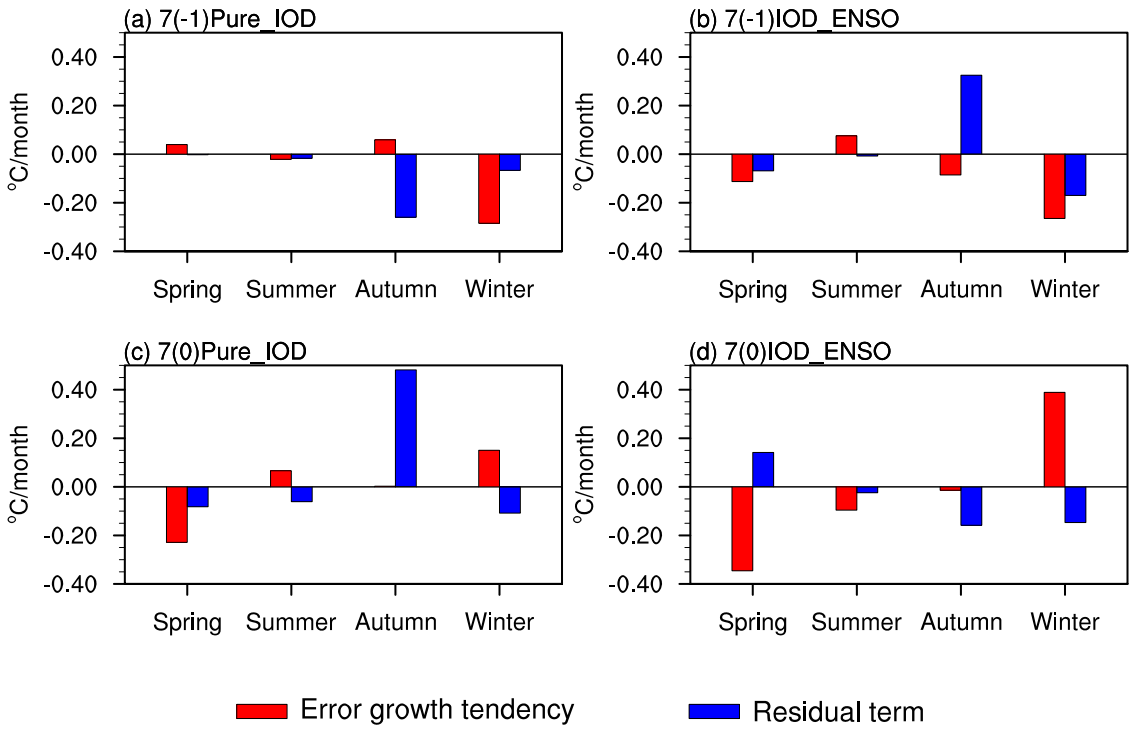

Figure 5. (a) Seasonal-dependent evolution of the error growth tendency (red bars) and residual term R (blue bars) in the growing phase of pure IOD events and (b) IOD events accompanied by ENSO, and (c) in the decaying phase of pure IOD events and (d) IOD events accompanied by ENSO, which are calculated based on the ensemble mean of the respective predictions (units: °C/month).

Due to the close link between the latent heat flux Q_L and the wind speed $|v_a|$ ($Q_L = \rho_a L_E C_E |v_a| [q_a - q_s(T_s)]$) [*Cayan*, 1992], the perturbed wind speed, related to the superimposed initial errors, in the eastern and western Indian Ocean is discussed to explore the contribution of the latent heat flux error to the seasonal-dependent development of prediction errors. Figure 12 shows that the perturbed wind speed in the eastern Indian Ocean is negative all year round with its largest absolute value in winter, indicating that the wind becomes weak under the effect of the superimposed initial errors. From the relationship between the latent heat flux and the wind speed, it can be inferred that the released latent heat flux in the eastern Indian Ocean decreases especially in winter and the latent heat flux error is positive; i.e., the amount of heat that the sea loses to the atmosphere decreases, resulting in an increase in the sea water temperature in the eastern Indian Ocean, which is largest in winter. Compared with the perturbed wind speed in the eastern Indian Ocean, the perturbed wind speed in the western Indian Ocean is small throughout the year and shows no seasonal dependence, which may result in a very small latent heat flux error and

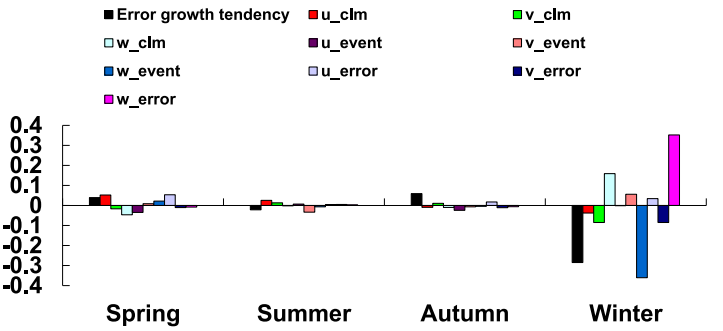

Figure 6. Error growth tendencies in four seasons (black bars) and their related oceanic temperature advection errors (colored bars), which are, respectively, the difference between the western and eastern Indian Ocean and based on the ensemble mean of the 15 predictions with initial errors that are most likely to cause the occurrence of the WPB in the growing phase of pure positive IOD events. The u, v, and w-clm represent the effect of the climatological mean state (zonal, meridional, and vertical temperature advections; $\overline{U}$, $\overline{V}$, and $\overline{W}$) on the error growth; u, v, and w-event denote the effect of anomalous temperature advection associated with positive IOD events (U^*, V^*, and W^*) on the error growth; and u, v, and w-error signify the effect of the temperature advection induced by the initial errors (U', V', and W') on the error growth (which indicates the effect of nonlinearity) (units: °C/month).

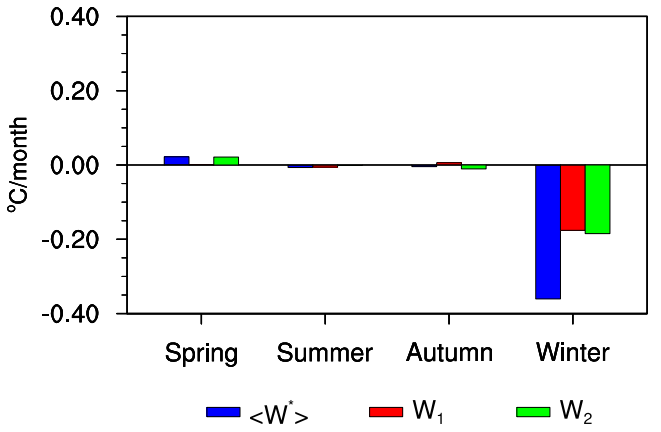

Figure 7. Seasonal-dependent evolution of $\langle W^* \rangle$, and its two components (W_1 and W_2), which are, respectively, the difference between the western and eastern Indian Ocean and are calculated based on the mean of the 15 individual predictions. Units: °C/month.

a small sea water temperature variation. As a result, the sea water temperature variation related to the perturbed wind speed shows an increase in the eastern Indian Ocean with its largest value in winter, and a very small variation in the western Indian Ocean, which may result in a decrease in the predicted IOD index in winter and advance the fastest growth of the negative prediction errors. To summarize, the seasonal-dependent distribution of the perturbed wind speed, especially in the eastern Indian Ocean, is favorable for the seasonal-dependent development of the prediction errors with the fastest error growth in winter through the effect of the latent heat flux error, resulting in the occurrence of the WPB.

The shortwave radiation error is another major thermodynamical process that contributes to the occurrence of the WPB. It is well known that shortwave radiation is closely related to the total cloud cover, and large

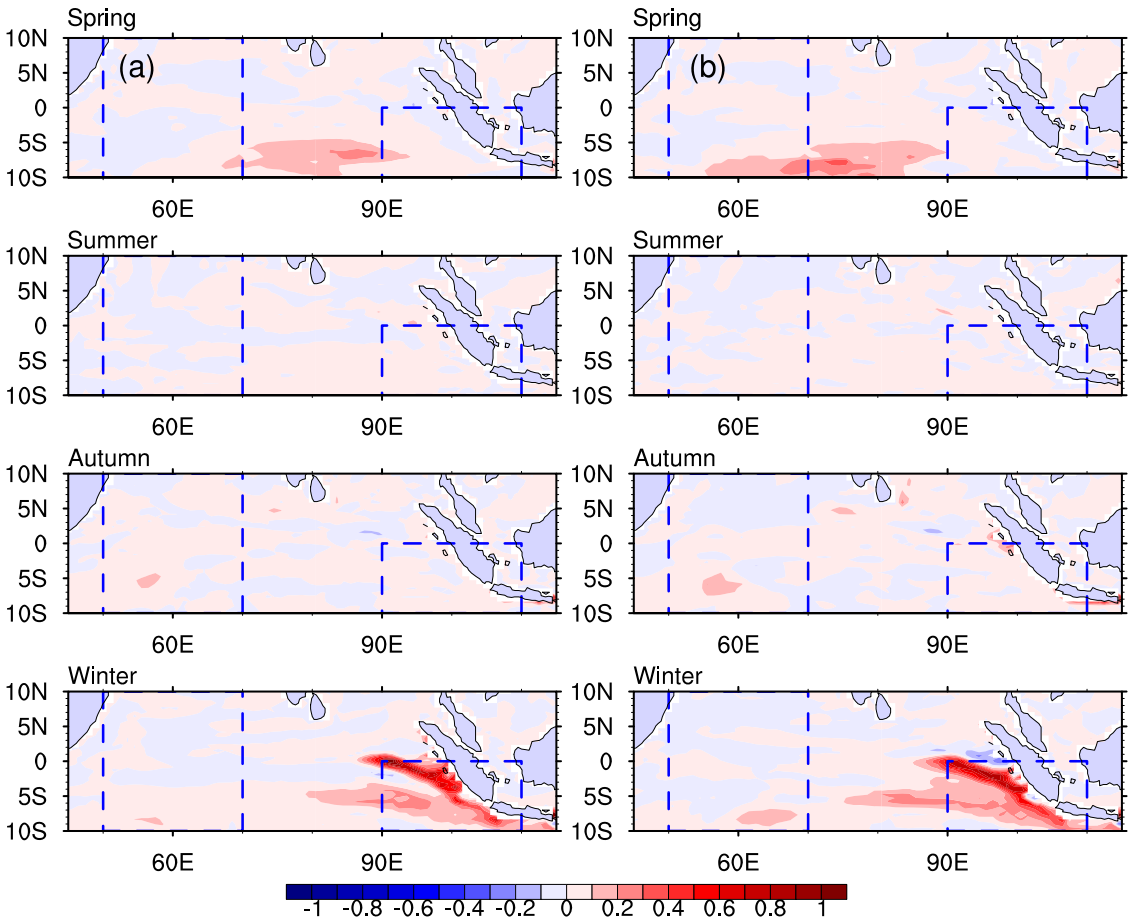

Figure 8. Composite spatial patterns of (a, left column) W_1 and (b, right column) W_2 in the tropical Indian Ocean in four seasons based on the mean of the 15 individual predictions. The blue boxes signify the west and east poles of positive IOD events. Units: °C/month.

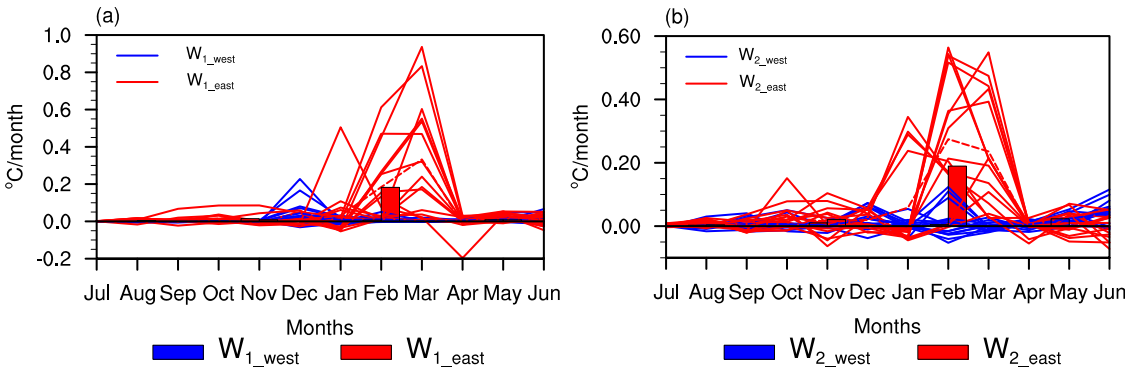

Figure 9. Time-dependent evolution of (a) W_1 and (b) W_2 in the west pole (blue lines) and east pole (red lines) of positive IOD events for different initial errors that cause the occurrence of the WPB in the growing phase of pure positive IOD events. Each solid line denotes every individual prediction, and its corresponding dotted line stands for their respective composition. The seasonal averages of the composition are denoted by the blue (red) bars in the west (east) pole of positive IOD events corresponding to August, November, February, and May in the horizontal axis (units: °C/month).

(small) cloud cover is often accompanied by small (large) shortwave radiation. Here we explore the distribution of the total cloud cover variation by analyzing the perturbed Walker circulation to explain the effect of the shortwave radiation error on the error growth. In winter, the rising (sinking) branch of the perturbed Walker circulation is located in the western (eastern) Indian Ocean, accompanied by the convergence (divergence) of water vapor; the increase (decrease) of the total cloud cover related to the water vapor change results in the decrease (increase) of the shortwave radiation and cooling (warming) of the sea water in the western (eastern) Indian Ocean, finally leading to the fast growth of negative prediction errors in winter (Figure 13). However, the shortwave radiation error induced by the perturbed Walker circulation in other seasons results in a warming (cooling or weak warming) in the western (eastern) Indian Ocean, which inhibits or weakly advances the error growth in the corresponding seasons. Therefore, the perturbed Walker circulation helps the shortwave radiation error to promote the seasonal-dependent development of the prediction errors, which show the largest error growth rate in winter. In conclusion, the shortwave radiation error, combined with the latent heat flux error, plays a dominant role in advancing the fastest error growth in winter from the viewpoint of thermodynamics.

The above discussions explain the physical mechanism of the WPB in the growing phase of pure positive IOD events from the viewpoints of the dynamics and the thermodynamics. The physical mechanism of the WPB for positive IOD events accompanied by ENSO is also explored in a similar way, revealing that the vertical temperature advection associated with the reference state positive IOD events and the latent heat flux error advance the fastest error growth in winter and induce the occurrence of the WPB (Figures 4b and 14). The major difference in the mechanism of the WPB for positive IOD events accompanied by ENSO from that for pure positive IOD events is reflected in the shortwave radiation error, which inhibits the error growth in winter for the events accompanied by ENSO. The related perturbed Walker circulation in winter is analyzed to explore the possible reasons for this difference (Figure 15). It is found that the distribution of the sinking and rising branches of the perturbed Walker circulation in the tropical Indian Ocean is different from that for pure positive IOD events, which results in a positive (negative) shortwave radiation error in the western (eastern) Indian Ocean. The related warming of the sea water in the western Indian Ocean and cooling in the eastern Indian Ocean inhibit the fast growth of the negative prediction errors in winter (Figure 4b). In short, the difference in the mechanism of the WPB for positive IOD events accompanied by ENSO from that for pure positive IOD events is mainly reflected in the shortwave radiation error, which may have a close relation with the perturbed atmospheric circulation in the tropical Indian Ocean associated with the effect of ENSO.

4.2. Prediction Bestriding the Winter in the Decaying Phase of Positive IOD Events

The analysis in section 3 suggests the existence of the WPB in the decaying phase of positive IOD events. In this section, predictions with start month 7 (0) are illustrated to explain the physical mechanism of the WPB in the decaying phase of positive IOD events. The pure positive IOD events are studied first, followed by a discussion of events accompanied by ENSO.

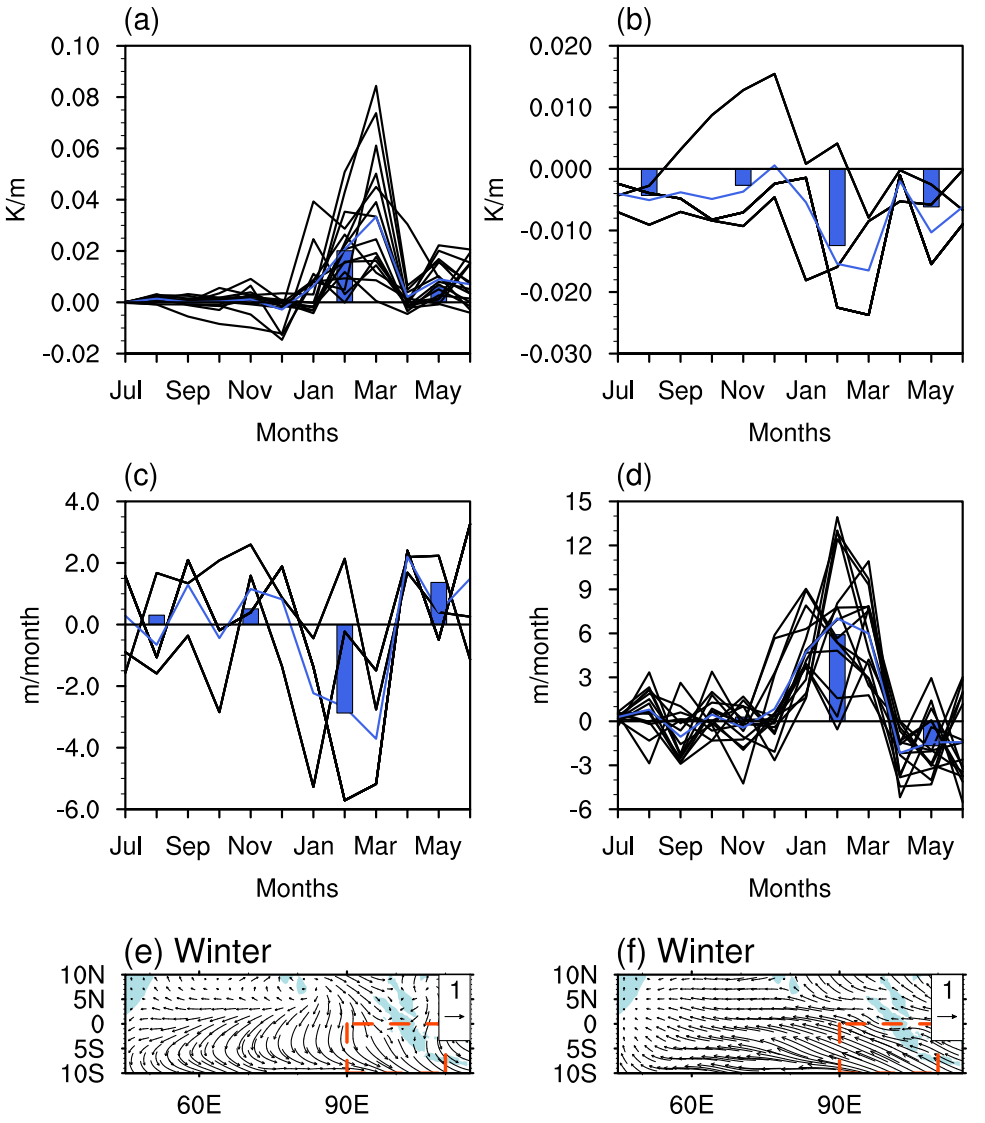

Figure 10. Time-dependent evolution of (a) $\langle \partial T'/\partial z \rangle$ (units: K/m), (b) $\langle \partial T^*/\partial z \rangle$ (units: K/m), (c) $\langle w^* \rangle$ (units: m/month), and (d) $\langle w' \rangle$ (units: m/month) in the east pole of positive IOD events for each individual prediction (black lines), their composition (blue lines) based on the mean of the 15 individual predictions, and the seasonal average of the composition (blue columns). (e) Composite spatial pattern of the anomalous wind in winter associated with the reference state IOD events, and (f) the composite spatial pattern of the perturbed wind in winter associated with the superimposed initial errors, which are respectively based on the mean of the 15 individual predictions; the red box denotes the east pole of positive IOD events (units: m/s).

Figure 4c shows the prediction errors of pure positive IOD events which have been superimposed with initial errors that are most likely to cause the occurrence of the WPB in its decaying phase. It is apparent that the prediction errors are mainly positive all year round and grow fastest in winter, indicating the existence of the WPB; the positive prediction errors may delay the decay of the predicted positive IOD events in winter. Physical processes that favor seasonal-dependent error growth and the occurrence of the WPB are chosen and analyzed from equation (7) based on the following criteria: first, the physical processes term should be positive in winter, which is the same sign as the prediction errors, indicating that these processes advance the rapid growth of the prediction errors in winter. Second, the advancement effect in winter on the error growth is larger than that in the other seasons. Furthermore, based on the above two criteria, only those physical processes whose magnitude is larger than half of the error growth tendency are seen as significant and analyzed in this study. As the term R does not meet the first criterion (Figures 5c and 5d), the physical processes that favor the seasonal-dependent development of prediction errors related to the WPB are explored from the viewpoints of dynamics and thermodynamics.

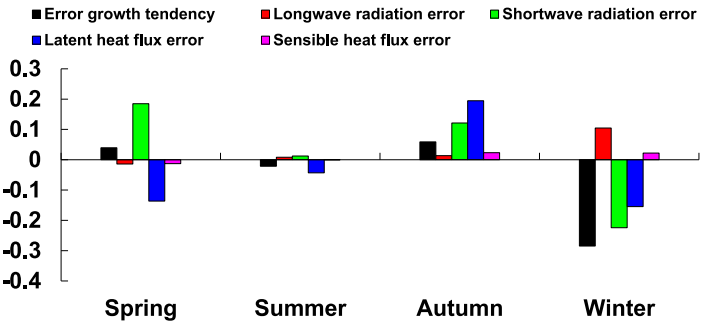

Figure 11. Error growth tendencies in four seasons (black bars) and the related four flux errors (colored bars), which are, respectively, based on the ensemble mean of the 15 predictions for initial errors that are most likely to cause the occurrence of the WPB in the growing phase of pure positive IOD events (units: °C/month).

The dynamical processes in equation (7) are analyzed for four seasons, which are calculated as the mean of seven individual predictions (Figure 16a). The horizontal temperature advection associated with the climatology plays a larger role than other oceanic dynamical processes in advancing the fast error growth in winter. However, the magnitudes of these processes are smaller than half of the error growth tendency, and are therefore considered insignificant in our study. We therefore focus only on the thermodynamical processes in the following discussions. Among the longwave radiation error, the shortwave radiation error, the latent heat flux error, and the sensible heat flux error, the latent heat flux error makes the largest contribution to advancing the fastest error growth in winter. Although the absolute value of the latent heat flux error in autumn is also large, its opposite sign to that of the prediction errors indicates its opposing effect on the error growth (Figure 16b). Therefore, the latent heat flux error dominates the thermodynamical effect on the seasonal-dependent development of the prediction errors, which show the fastest growth in winter.

Due to the close relation between the latent heat flux and the wind speed ($Q_L=\rho_a L_E C_E|v_a|[q_a-q_s(T_s)]$), the perturbed wind speed in the western and eastern Indian Ocean is further explored to determine the seasonal distribution of the latent heat flux error and its contribution to the occurrence of the WPB (Figure 17). The perturbed wind speed in the western (eastern) Indian Ocean is negative (positive) in winter, indicating that the wind becomes weak (strong) under the effect of initial errors. According to the relation $Q_L=\rho_a L_E C_E|v_a|[q_a-q_s(T_s)]$, the released latent heat flux decreases (increases) in the western (eastern) Indian Ocean, resulting in warming (cooling) of the sea water in the western (eastern) Indian Ocean, which advances the fast growth of positive prediction errors in winter. However, the perturbed wind speed in other seasons is weak, and the related latent heat flux error has little effect on the error growth. In conclusion, the seasonal distribution of the perturbed wind speed makes a large contribution to the fastest error growth in winter through the effect of the latent heat flux error, and is favorable for the occurrence of the WPB.

The previous discussions show that the latent heat flux error plays a dominant role in inducing the occurrence of the WPB for pure positive IOD events, and the physical mechanism of the WPB for positive IOD events accompanied by ENSO is also analyzed. Figure 18 shows that the latent heat flux error and the shortwave radiation error make a large contribution to the seasonal-dependent development of the prediction errors, which show the fastest error growth in winter (Figure 4d). The effect of the shortwave radiation error on the error growth in winter is different for positive IOD events accompanied by ENSO compared with events unaccompanied by ENSO; the former case makes a larger contribution to the fast error growth in winter. Further work shows that the different distribution of the perturbed Walker circulation, especially in the western Indian Ocean (near

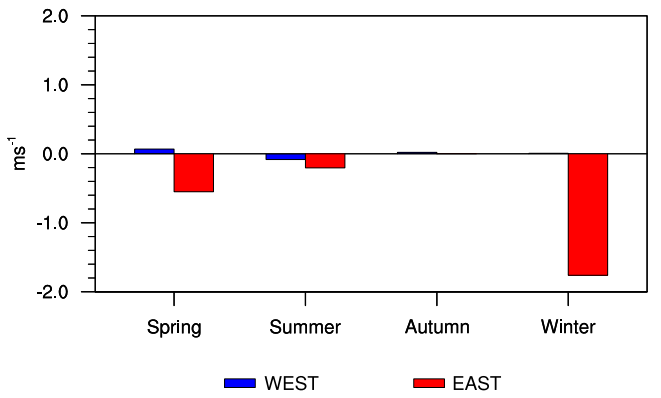

Figure 12. Seasonal-dependent evolution of the perturbed wind speed in the west and east poles of positive IOD events, which are calculated based on the mean of the 15 individual predictions (units: m/s).

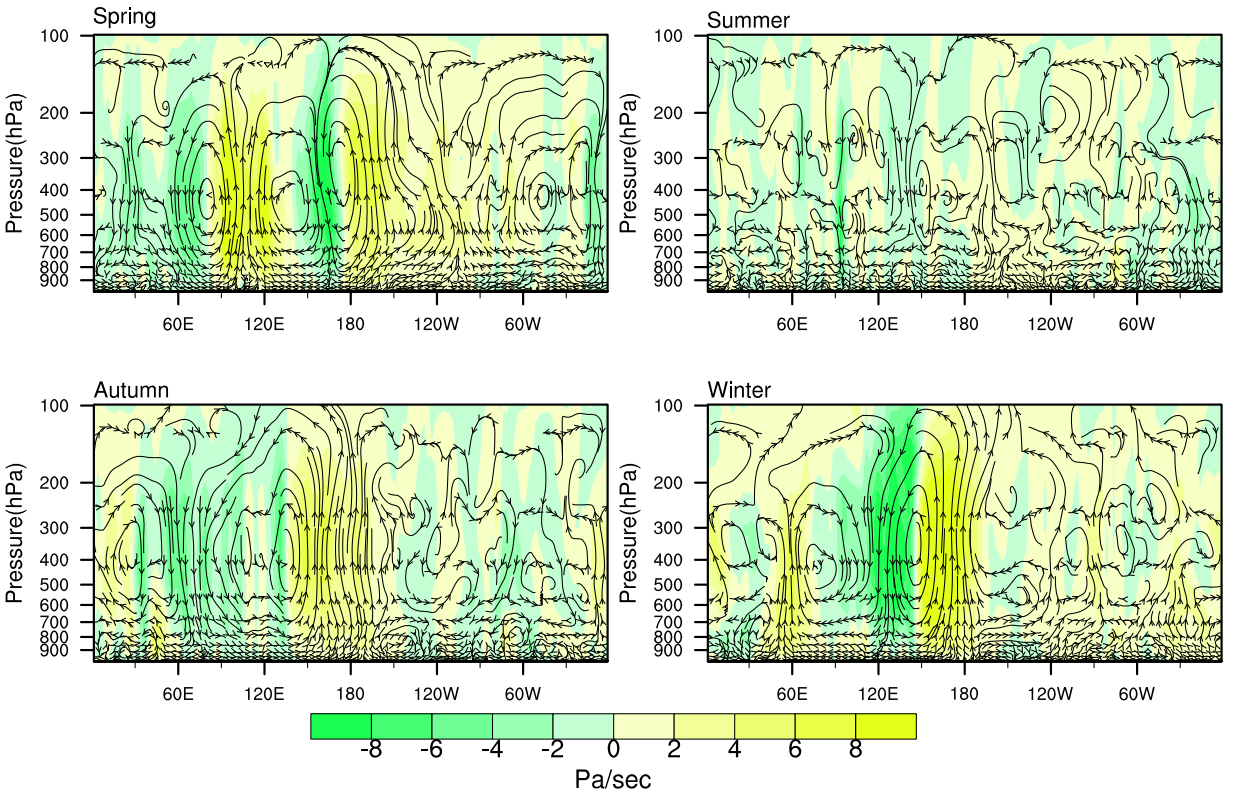

Figure 13. The perturbed Walker circulation (arrow; the vertical velocity component has been multiplied by 400) and the perturbed vertical velocity (shaded; units: 1/400 Pa/s) in four seasons, which are based on the ensemble mean of the 15 predictions for initial errors that are most likely to cause the occurrence of the WPB in the growing phase of pure positive IOD events. The zonal average is taken over 10°S–0° in the east pole of positive IOD events, and over 10°S–10°N in other regions.

50°E) results in a different effect of the shortwave radiation error on the positive error growth in winter, which may have a close relation to the effect of ENSO (Figure 19).

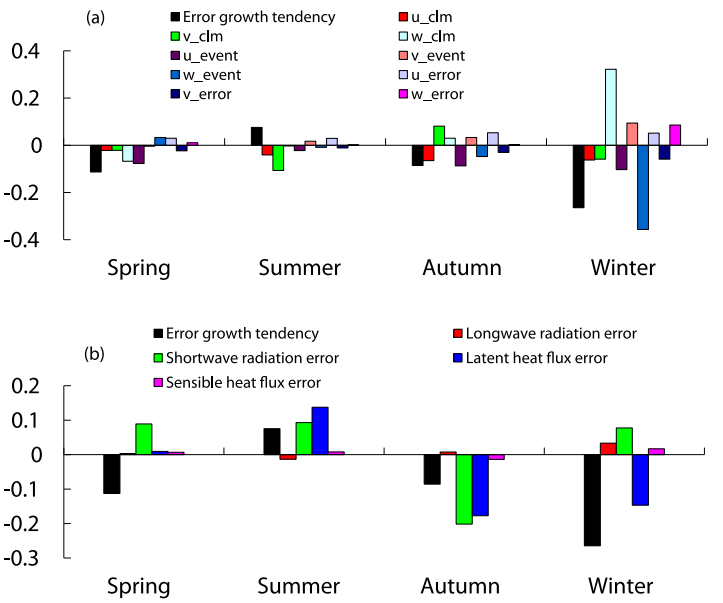

Figure 14. (a and b) Same as Figures 6 and 11, respectively, but for the mean of integrations for initial errors that are most likely to cause the occurrence of the WPB in the growing phase of positive IOD events accompanied by ENSO (units: °C/month).

5. Summary and Conclusions

The Indian Ocean dipole (IOD) is an important ocean-atmosphere coupled phenomenon that has a strong effect on global climate. In this study, using the GFDL CM2p1 coupled model, the winter predictability barrier (WPB) described by *Luo et al.* [2007], in which the initial errors show a significant seasonal-dependent evolution with the fastest error growth in winter, is found to exist in the model not only in the growing phase of positive IOD events but also in the decaying phase. In the perfect model predictability experiments, the GFDL

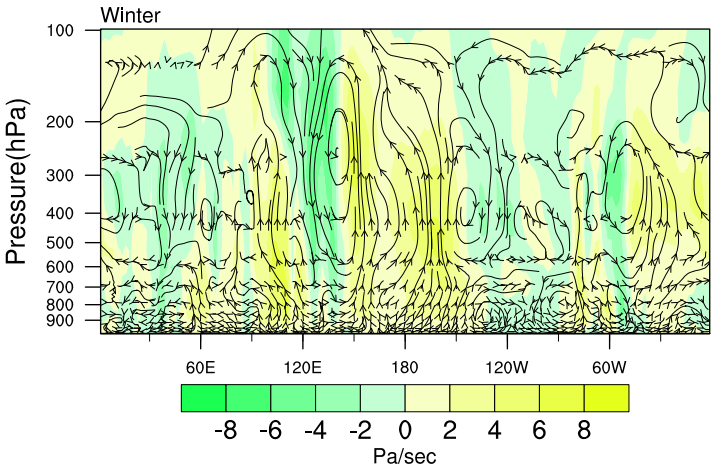

Figure 15. Same as Figure 13, but for winter only, based on the ensemble mean of the predictions for initial errors that are most likely to cause the occurrence of the WPB in the growing phase of positive IOD event accompanied by ENSO.

CM2p1 coupled model is taken to be a perfect model and the prediction errors are caused only by initial errors. By superimposing different initial errors of the same magnitude onto sea temperatures at the sea surface and at 95 m depth and then integrating for 12 months from six start months, initial errors that are most likely to cause the occurrence of the WPB were selected. Based on the evolution of these initial errors, the physical mechanism of the WPB was explored using the sea water temperature tendency equation for different developmental phases of positive IOD events from the viewpoints of dynamics and thermodynamics.

In the growing phase of pure positive IOD events, the vertical temperature advection associated with the reference state IOD events plays a dominant role in advancing the fastest error growth in winter in terms of dynamics, which is the combined effect of the following two terms: the vertical advection effect of the anomalous vertical velocity on the perturbed sea water temperature, and the vertical advection effect of the perturbed vertical velocity on the anomalous sea water temperature. For thermodynamics, the latent heat flux error and the shortwave radiation error cause the fastest error growth in winter and favor the occurrence of the WPB. The seasonal-dependent distribution of the perturbed wind speed, especially in the eastern Indian Ocean, is favorable for the seasonal-dependent development of the prediction errors, with the fastest growth in winter, through the effect of the latent heat flux error. Moreover, the perturbed Walker circulation aids the shortwave radiation error in promoting the fastest error growth in winter, finally leading to the occurrence of the WPB. The physical mechanism of the WPB for positive IOD events accompanied by ENSO is also analyzed. It is shown that the main difference between the physical mechanism in this case and that in the previous discussion is reflected in the shortwave radiation error, which inhibits error growth in winter for events accompanied by ENSO. This effect of the shortwave radiation error may be closely related to the perturbed atmospheric circulation in the tropical Indian Ocean associated with the effect of ENSO.

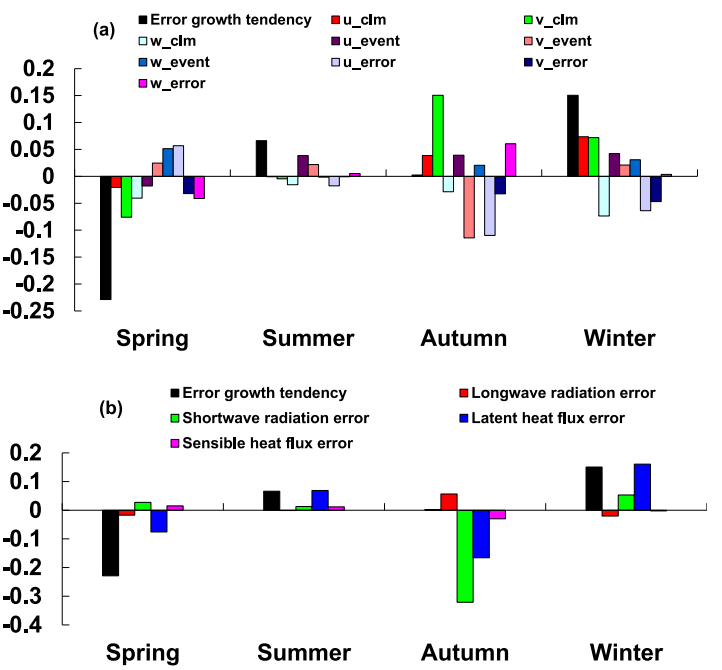

Figure 16. (a and b) Same as Figures 6 and 11, respectively, but for the mean of integrations for initial errors that are most likely to cause the occurrence of the WPB in the decaying phase of pure positive IOD events (units: °C/month).

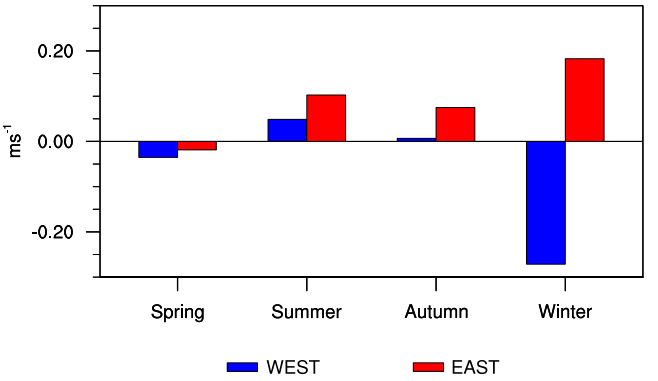

Figure 17. Same as Figure 12, but for the mean of the seven individual predictions with initial errors that are most likely to cause the WPB in the decaying phase of pure IOD events (units: m/s).

In the decaying phase of pure positive IOD events, since the dynamics have an insignificant effect on the error growth in winter, the occurrence of the WPB is mainly due to the effect of the latent heat flux error in terms of thermodynamics, which in turn is strongly related to the seasonal-dependent distribution of the perturbed wind speed. The mechanism of the WPB for positive IOD events accompanied by ENSO is studied in more detail. It is found that the shortwave radiation error greatly advances the fastest error growth in winter, in addition to the latent heat flux error; this is the main difference in the physical mechanism of the WPB for positive IOD events accompanied by ENSO from that for pure positive IOD events. The different distribution of the perturbed Walker circulation, especially in the western Indian Ocean (near 50°E), results in the different effect of the shortwave radiation error on the positive error growth in winter.

Feng et al. [2014] showed that the variance of the IOD index in the GFDL CM2p1 model is smallest in winter, indicating that the signal of IOD events is weakest. The combination of the weakest signal and fastest error growth means that the signal-to-noise ratio is smallest in winter, so the IOD events have the lowest predictability in winter. This indicates that, if the noises are described by the prediction errors in the present study, they, due to their winter largest growth, may be most likely to conceal the signal associated with IOD events in winter, and then result in the occurrence of the WPB phenomenon. That is to say, the measurement signal-to-noise ratio can also demonstrate the WPB of IOD in the GFDL CM2p1 model, as revealed by the growth of prediction errors caused by initial errors.

Previous studies revealed that ENSO has a large impact on the development of IOD events, and often causes a stronger IOD [*Song et al*., 2007]. The discussion in this study showed that ENSO also affects the development of the prediction errors of IOD events through the effect of the shortwave radiation error. However, the detailed effects of ENSO on the predictability of IOD events require further analysis in future work, which would aid our understanding of the interaction between the IOD and ENSO.

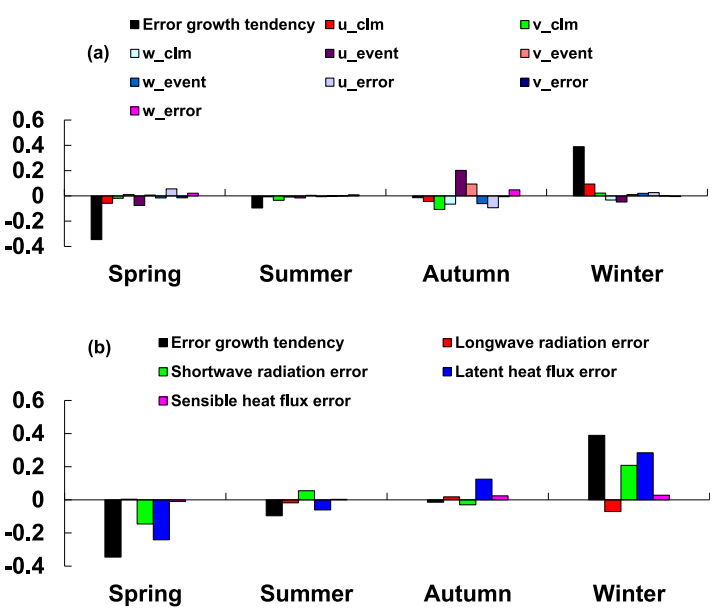

Figure 18. (a and b) Same as Figures 6 and 11, respectively, but for the mean of integrations for initial errors that are most likely to cause the occurrence of the WPB in the decaying phase of positive IOD events accompanied by ENSO (units: °C/month).

In the perfect model predictability experiment hypothesis, initial errors superimposed on the sea temperatures at the sea surface and at 95 m depth cause the occurrence of the WPB, and the dominant pattern of these initial errors shows an eastern-western dipole mode. Previous studies have demonstrated that the initial errors causing significant prediction uncertainties for coupled ocean–atmospheric modes (e.g., ENSO events, Kuroshio

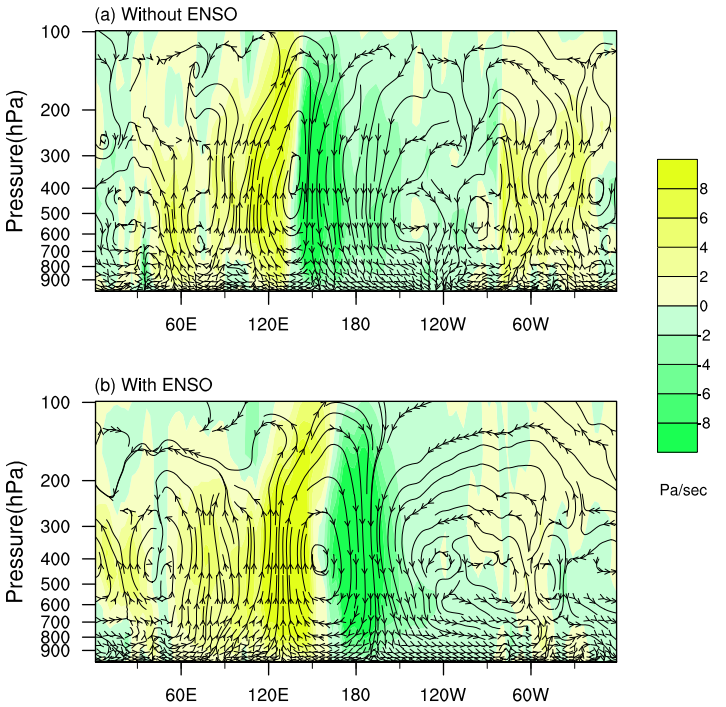

Figure 19. The perturbed Walker circulation (arrow; the vertical velocity component has been multiplied by 400) and the perturbed vertical velocity (shaded; units: 1/400 Pa/s) in winter. (a) Based on the ensemble mean of the seven predictions for initial errors that are most likely to cause the occurrence of the WPB in the decaying phase of pure positive IOD events; (b) based on the ensemble mean of the 15 predictions for initial errors that are most likely to cause the occurrence of the WPB in the decaying phase of positive IOD events accompanied by ENSO. The zonal average is taken over 10°S–0° in the east pole of positive IOD events, and over 10°S–10°N in other regions.

Large Meander, Atlantic and Pacific blockings, etc.) may have dynamical growth behavior similar to the events themselves [*Yu et al*., 2009; *Jiang and Wang*, 2010; *Duan et al*., 2012; *Wang et al*., 2012]. This conclusion may be also applicable to the error growth in IOD events. That is, the initial errors in the sea temperature may have dynamical growth behavior similar to IOD events, and therefore cause the aforementioned perturbations in the wind speed/Walker circulation/vertical velocity/vertical temperature gradient discussed in section 4; however, the detailed mechanisms in this process still need further exploration. Besides, the large values of those dipole-pattern initial errors concentrate within a few areas; then can these areas provide useful information about the sensitive areas of targeted observations for IOD events? This motivates us to explore the sensitive areas of positive IOD predictions from the sea temperatures at the sea surface and at 95 m depth in future study. More observations in these areas could help reduce initial errors, which therefore decreases the prediction errors in winter and in turn weaken the WPB.

Acknowledgments
Readers can access the data used in this paper by email: duanws@lasg.iap.ac.cn. This work was jointly sponsored by the National Public Benefit (Meteorology) Research Foundation of China (GYHY201306018) and the National Basic Research Program of China (2012CB955202).

References

Abram, N. J., M. K. Gagan, M. T. McCulloch, J. Chappell, and W. S. Hantoro (2003), Coral reef death during the 1997 Indian Ocean dipole linked to Indonesian wildfires, *Science*, *301*(5635), 952–955.

Annamalai, H., and R. Murtugudde (2004), Role of the Indian Ocean in regional climate variability, in *Earth Climate: The Ocean-Atmosphere Interaction*, vol. 147, edited by C. Wang, S. P. Xie, and J. A. Carton, pp. 213–246, AGU, Washington, D. C., doi:10.1029/147GM13.

Annamalai, H., J. Potemra, R. Murtugudde, and J. P. Mccreary (2005), Effect of preconditioning on the extreme climate events in the tropical Indian Ocean, *J. Clim.*, *18*(17), 3450–3469.

Ansell, T., C. J. C. Reason, and G. Meyers (2000), Variability in the tropical southeast Indian Ocean and links with southeast Australian winter rainfall, *Geophys. Res. Lett.*, *27*(24), 3977–3980.

Ashok, K., Z. Guan, and T. Yamagata (2001), Impact of the Indian Ocean dipole on the relationship between the Indian monsoon rainfall and ENSO, *Geophys. Res. Lett.*, *28*(23), 4499–4502.

Ashok, K., Z. Guan, and T. Yamagata (2003), Influence of the Indian Ocean dipole on the Australian winter rainfall, *Geophys. Res. Lett.*, *30*(15), 1821, doi:10.1029/2003GL017926.

Behera, S. K., J. J. Luo, S. Masson, P. Delecluse, S. Gualdi, A. Navarra, and T. Yamagata (2005), Paramount impact of the Indian Ocean dipole on the East African short rains: A CGCM study, *J. Clim.*, *18*(21), 4514–4530.

Behera, S. K., J. J. Luo, S. Masson, S. A. Rao, H. Sakuma, and T. Yamagata (2006), A CGCM study on the interaction between IOD and ENSO, *J. Clim.*, *19*(9), 1688–1705.

Birkett, C., R. Murtugudde, and T. Allan (1999), Indian Ocean climate event brings floods to East Africa's lakes and the Sudd Marsh, *Geophys. Res. Lett.*, *26*(8), 1031–1034.

Black, E., J. Slingo, and K. R. Sperber (2003), An observational study of the relationship between excessively strong short rains in coastal east Africa and Indian Ocean SST, *Mon. Weather Rev.*, *131*(1), 74–94.

Cai, W., H. H. Hendon, and G. Meyers (2005), Indian Ocean dipole like variability in the CSIRO Mark 3 coupled climate model, *J. Clim.*, *18*(10), 1449–1468.

Cai, W., T. Cowan, and A. Sullivan (2009), Recent unprecedented skewness towards positive Indian Ocean Dipole occurrences and its impact on Australian rainfall, *Geophys. Res. Lett.*, *36*, L11705, doi:10.1029/2009GL037604.

Cayan, D. R. (1992), Latent and sensible heat flux anomalies over the northern oceans: Driving the sea surface temperature, *J. Phys. Oceanogr.*, *22*, 859–879.
Clark, C. O., P. J. Webster, and J. E. Cole (2003), Interdecadal variability of the relationship between the Indian Ocean zonal mode and East African coastal rainfall anomalies, *J. Clim.*, *16*(3), 548–554.
Delworth, T. L., et al. (2006), GFDL's CM2 global coupled climate models. Part I: Formulation and simulation characteristics, *J. Clim.*, *19*, 643–674.
Duan, W., X. Liu, K. Zhu, and M. Mu (2009), Exploring the initial errors that cause a significant "spring predictability barrier" for El Niño events, *J. Geophys. Res.*, *114*, C04022, doi:10.1029/2008JC004925.
Duan, W., Y. Yu, H. Xu, and P. Zhao (2012), Behaviors of nonlinearities modulating the El Niño events induced by optimal precursory disturbances, *Clim. Dyn.*, *40*(5–6), 1399–1413.
Feng, R., and W. S. Duan (2014), The spatial patterns of initial errors related to the "winter predictability barrier" of the Indian Ocean dipole, *Atmos. Oceanic Sci. Lett.*, *7*(5), 406–410, doi:10.3878/j.issn.1674-2834.14.0018.
Feng, R., M. Mu, and W. Duan (2014), Study on the "winter persistence barrier" of Indian Ocean dipole events using observation data and CMIP5 model outputs, *Theor. Appl. Climatol.*, *118*(3), 523–534, doi:10.1007/s00704-013-1083-x.
GFDL Global Atmospheric Model Development Team (2004), The new GFDL global atmosphere and land model AM2-LM2: Evaluation with prescribed SST simulations, *J. Clim.*, *17*, 4641–4673.
Gnanadesikan, A., K. W. Dixon, S. M. Griffies, V. Balaji, M. Barreiro, J. A. Beesley, W. F. Cooke, T. L. Delworth, R. Gerdes, and M. J. Harrison (2006), GFDL's CM2 global coupled climate models. Part: The baseline ocean simulation, *J. Clim.*, *19*(5), 675–697, doi:10.1175/JCLI3630.1.
Griffies, S. M. (2009), Elements of MOM4p1: GFDL Ocean Group, *Tech. Rep. 6*, NOAA/Geophys. Fluid Dyn. Lab., Princeton, N. J.
Guan, Z., and T. Yamagata (2003), The unusual summer of 1994 in East Asia: IOD teleconnections, *Geophys. Res. Lett.*, *30*(10), 1544, doi:10.1029/2002GL016831.
Hong, C. C., T. Li, L. Ho, and J. S. Kug (2008), Asymmetry of the Indian Ocean dipole. Part I: Observational analysis, *J. Clim.*, *21*(18), 4834–4848.
Jiang, Z., and D. Wang (2010), A study on precursors to blocking anomalies in climatological flows by using conditional nonlinear optimal perturbations, *Q. J. R. Meteorol. Soc.*, *136*(650), 1170–1180.
Kaplan, A., M. A. Cane, Y. Kushnir, A. C. Clement, M. B. Blumenthal, and B. Rajagopalan (1998), Analyses of global sea surface temperature 1856–1991, *J. Geophys. Res.*, *103*(C9), 18,567–18,589, doi:10.1029/97JC01736.
Krishnamurthy, V., and B. P. Kirtman (2003), Variability of Indian Ocean: Relation to monsoon and ENSO, *Q. J. R. Meteorol. Soc.*, *129*(590), 1623–1646.
Lareef, Z., A. S. Rao, and T. Yamagata (2003), Modulation of Sri Lankan Maha rainfall by the Indian Ocean dipole, *Geophys. Res. Lett.*, *30*(2), 1063, doi:10.1029/2002GL015639.
Lau, K. M., and S. Yang (1996), The Asian monsoon and predictability of the tropical ocean-atmosphere system, *Q. J. R. Meteorol. Soc.*, *122*, 945–957.
Lau, N. C., and M. J. Nath (2004), Coupled GCM simulation of atmosphere-ocean variability associated with zonally asymmetric SST changes in the tropical Indian Ocean, *J. Clim.*, *17*(2), 245–265.
Li, T., Y. Zhang, E. Lu, and D. Wang (2002), Relative role of dynamic and thermodynamic processes in the development of the Indian Ocean dipole: An OGCM diagnosis, *Geophys. Res. Lett.*, *29*(23), 2110, doi:10.1029/2002GL015789.
Li, T., B. Wang, C. P. Chang, and Y. Zhang (2003), A theory for the Indian Ocean dipole-zonal mode, *J. Atmos. Sci.*, *60*(17), 2119–2135.
Luo, J. J., S. Masson, S. Behera, S. Shingu, and T. Yamagata (2005), Seasonal climate predictability in a coupled OAGCM using a different approach for ensemble forecasts, *J. Clim.*, *18*(21), 4474–4497.
Luo, J. J., S. Masson, S. Behera, and T. Yamagata (2007), Experimental forecasts of the Indian Ocean dipole using a coupled OAGCM, *J. Clim.*, *20*(10), 2178–2190, doi:10.1175/JCLI4132.1.
Mu, M., W. S. Duan, and B. Wang (2003), Conditional nonlinear optimal perturbation and its applications, *Nonlinear Processes Geophys.*, *10*, 493–501.
Mu, M., W. S. Duan, and B. Wang (2007), Season-dependent dynamics of nonlinear optimal error growth and El Niño-Southern Oscillation predictability in a theoretical model, *J. Geophys. Res.*, *112*, D10113, doi:10.1029/2005JD006981.
Murtugudde, R., J. P. McCreary, and A. J. Busalacchi (2000), Oceanic processes associated with anomalous events in the Indian Ocean with relevance to 1997–1998, *J. Geophys. Res.*, *105*(C2), 3295–3306.
Paulson, C. A., and J. J. Simpson (1977), Irradiance measurements in upper ocean, *J. Phys. Oceanogr.*, *7*(6), 952–956.
Rao, S. A., S. K. Behera, Y. Masumoto, and T. Yamagata (2002), Interannual subsurface variability in the tropical Indian Ocean with a special emphasis on the Indian Ocean Dipole, *Deep Sea Res., Part II*, *49*, 1549–1572.
Saji, N. H., and T. Yamagata (2003a), Structure of SST and surface wind variability during Indian Ocean dipole mode events: COADS observations, *J. Clim.*, *16*(16), 2735–2751.
Saji, N. H., and T. Yamagata (2003b), Possible impacts of Indian Ocean dipole mode events on global climate, *Clim. Res.*, *25*(2), 151–169.
Saji, N. H., B. N. Goswami, P. N. Vinayachandran, and T. Yamagata (1999), A dipole mode in the tropical Indian Ocean, *Nature*, *401*(6751), 360–363.
Shi, L., H. H. Hendon, O. Alves, J. J. Luo, M. Balmaseda, and D. Anderson (2012), How predictable is the Indian Ocean dipole?, *Mon. Weather Rev.*, *140*(12), 3867–3884, doi:10.1175/MWR-D-12-00001.1.
Shinoda, T., M. A. Alexander, and H. H. Hendon (2004), Remote response of the Indian Ocean to interannual SST variations in the tropical Pacific, *J. Clim.*, *17*(2), 362–372.
Song, Q., G. A. Vecchi, and A. J. Rosati (2007), Indian Ocean variability in the GFDL coupled climate model, *J. Clim.*, *20*, 2895–2916, doi:10.1175/JCLI4159.1.
Stouffer, R. J., et al. (2006), GFDL's CM2 global coupled climate models. Part IV: Idealized climate response, *J. Clim.*, *19*, 723–740.
Torrence, C., and P. J. Webster (1998), The annual cycle of persistence in the El Niño-Southern Oscillation, *Q. J. R. Meteorol. Soc.*, *125*, 1985–2004.
Vecchi, G. A., and D. E. Harrison (2004), Interannual Indian rainfall variability and Indian Ocean sea surface temperature anomalies, in *Earth's Climate: The Ocean-Atmosphere Interaction, Geophys. Monogr. Ser.*, edited by C. Wang, S. P. Xie, and J. A. Carton, pp. 247–259, AGU, Washington, D. C.
Vinayachandran, P. N., S. Iizuka, and T. Yamagata (2002), Indian Ocean dipole mode events in an ocean general circulation model, *Deep Sea Res., Part II*, *49*(7), 1573–1596.
Wajsowicz, R. C. (2004), Climate variability over the tropical Indian Ocean sector in the NSIPP seasonal forecast system, *J. Clim.*, *17*(24), 4783–4804.

Wajsowicz, R. C. (2005), Potential predictability of tropical Indian Ocean SST anomalies, *Geophys. Res. Lett.*, *32*, L24702, doi:10.1029/2005GL024169.

Wajsowicz, R. C. (2007), Seasonal-to-interannual forecasting of tropical Indian Ocean sea surface temperature anomalies: Potential predictability and barriers, *J. Clim.*, *20*(13), 3320–3343, doi:10.1175/JCLI4162.1.

Wang, Q., M. Mu, and H. A. Dijkstra (2012), Application of the conditional nonlinear optimal perturbation method to the predictability study of the Kuroshio large meander, *Adv. Atmos. Sci.*, *29*(1), 118–134.

Webster, P. J. (1995), The annual cycle and the predictability of the tropical coupled ocean-atmosphere system, *Meteorol. Atmos. Phys.*, *56*(1–2), 33–55.

Webster, P. J., and S. Yang (1992), Monsoon and ENSO: Selectively interactive systems, *Q. J. R. Meteorol. Soc.*, *118*, 877–926.

Webster, P. J., A. M. Moore, J. P. Loschnigg, and R. R. Leben (1999), Coupled ocean-atmosphere dynamics in the Indian Ocean during 1997–1998, *Nature*, *401*(6751), 356–360.

Weller, E., and W. Cai (2013), Asymmetry in the IOD and ENSO teleconnection in a CMIP5 model ensemble and its relevance to regional rainfall, *J. Clim.*, *26*, 5139–5149.

Wittenberg, A. T., A. Rosati, N. C. Lau, and J. J. Ploshay (2006), GFDL's CM2 global coupled climate models. Part III: Tropical pacific climate and ENSO, *J. Clim.*, *19*(5), 698–722, doi:10.1175/JCLI3631.1.

Yamagata, T., S. K. Behera, J. J. Luo, S. Masson, M. R. Jury, and S. A. Rao (2004), Coupled ocean-atmosphere variability in the tropical Indian Ocean, in *Earth's Climate*, edited by C. Wang, S. P. Xie, and J. A. Carton, pp. 189–212, AGU, Washington, D. C., doi:10.1029/147GM12.

Yu, Y., W. S. Duan, and M. Mu (2009), Dynamics of nonlinear error growth and season-dependent predictability of El Niño events in the Zebiak-Cane model, *Q. J. R. Meteorol. Soc.*, *135*, 2146–2160, doi:10.1002/qj.526.

Zhao, M., and H. H. Hendon (2009), Representation and prediction of the Indian Ocean dipole in the POAMA seasonal forecast model, *Q. J. R. Meteorol. Soc.*, *135*(639), 337–352, doi:10.1002/qj.370.

Zhong, A., H. H. Hendon, and O. Alves (2005), Indian Ocean variability and its association with ENSO in a global coupled model, *J. Clim.*, *18*(17), 3634–3649.